ISSN 0915-633X

NATIONAL INSTITUTE FOR FUSION SCIENCE

Pellet Ablation in the Large Helical Device

Boris V. Kuteev

(Received – Sep. 30, 1993)

NIFS-260 Nov. 1993

RESEARCH REPORT
NIFS Series

NAGOYA, JAPAN

Pellet Ablation in Large Helical Device

Boris V. Kuteev*

Technical University, Polytechnicheskaya 29, 195251 St. Petersburg, Russia

Abstract

In the program of physical studies on the Large Helical Device (LHD) injection of several hydrogen and deuterium pellets is foreseen. Injection of impurity pellets also may be useful for the plasma diagnostics. The pellet penetration into the LHD plasma is analyzed. In part 1, the present status of the ablation theory and experiment is discussed and an ablation model is formulated. It takes into account energy distribution of the particles (both electrons and ions) participating in the ablation process, electrostatic effects of the cloud charging and changes of the pellet form during ablation. Plasma shielding effects are not significant in the ablation. The ablation model is compared with the experiments on T-10, JET, TFTR, Heliotron-E and Tore Supra in part 2. Finally, in part 3, several regimes of the pellet injection into the LHD plasma are simulated including multiple-pellet sequence injection. Optimization of the injection regime is discussed.

Keywords: pellet, ablation, toroidal acceleration, Large Helical Device, plasma

Part 1. Pellet Ablation Model

1.1. Introduction

The problem of hydrogen pellet ablation in thermonuclear plasma has been analyzed intensively since the neutral shielding model was proposed [1]. One-dimensional approach with monoenergetic electron heat flux has been developed in References 1-3 with detailed analysis of the hydrodynamic parameters of the neutral cloud. As a result the formula for the ablation rate *dN/dt* (atom/s) has been proposed

$$dN/dt = 1.12\times10^{16} n_e^{0.333} T_e^{1.64} r_p^{1.333} M_i^{-0.333} \qquad (1)$$

where n_e and T_e are the electron density (in cm^{-3}) and temperature (in eV), r_p is the pellet radius (in cm), M_i is mass of the pellet material in atomic units. Below all the units are in CGS-system except temperature and energy that are in eV.

Although a reasonable agreement of this formula with the tokamak and stellarator experiments has been demonstrated, it was pointed out by several investigators [4,5,7] that this agreement may be

* Guest Researcher to National Institute for Fusion Science, Nagoya, Japan.

occasionally originated from a compensation of several factors acting in opposite directions. First significant factor is the Maxwellian distribution of the electrons that increases the heat flux ablating the pellet [4-10]. However, this increase looks as if too large and several effects have been proposed that may make the ablation rate lower again. Two-dimensional nature of the ablation process [4,5,11] is a possible phenomenon decreasing the erosion rate in a factor of 2 [5]. Another factor is the electrostatic shielding of the heat flux by the double layer at the boundary of hot and cold plasmas [12]. Its influence on ablation may be of order 2 as well. Several authors have analyzed the plasma shielding as a possible factor decreasing the ablation rate [4-8,13-15]. However, experimentally such an influence was not confirmed [8]. It is recognized that the effect of the magnetic shielding analyzed in References 16-18 is also weak in the real tokamak conditions.

Any ablation model, including the effects of the energy distribution, two-dimensional ablation, and electrostatic and plasma shielding, has not yet succeeded in giving the ablation values close to the formula (1). There are several problems with the ion influence on the ablation rate as well. One dimensional approach [6, 19, 20] should be significantly revised in the case of two-dimensional analysis, because the regions with dominant electron and ion ablations are separated on the pellet surface. It is also necessary to analyze the modification of the pellet shape during ablation that was only briefly discussed in Reference 5 and was significantly developed in the case of impurity pellet in Reference 11.

The main purpose of this paper is to establish (develop) a two-dimensional model with electron and ion ablation and the pellet shape modification during ablation taken into account.

1.2 General Ideas and Electron Ablation

First, we shall analyze ablation of the initially spherical hydrogen pellet with radius r_{po} moving across the magnetic field lines with a velocity v_p. For the typical experimental conditions (r_{po}=0.05-0.2 cm and v_p=10^5-3×10^5 cm/s) the characteristic time of changing the ablating plasma r_{po}/v_p is approximately equal to 10^{-6} s. This time is much less than the time necessary for cooling of the magnetic surface at which the pellet is located except some special conditions on a rational magnetic surface [6,21]. We shall not discuss this situation below and assume that the background plasma is not disturbed by the pellet and it has electron temperature T_e and density n_e far away from the pellet. For the ions we shall consider two different species: thermal ions with temperature T_i and density n_i and hot ions generated by neutral beam heating (NBI) with total power P_b and the beam energy E_b.

The background plasma is assumed to be Maxwellian for the thermal electrons and ions with isotropic distribution function in the forms

$$f_e(v)=\left(m_e/2\pi T_e\right)^{3/2} n_e \exp\left(-m_e v^2/2T_e\right) \qquad (2)$$

$$f_i(v)=\left(m_i/2\pi T_i\right)^{3/2} n_i \exp\left(-m_i v^2/2T_i\right) \tag{3}$$

Effects on the pellet ablation of a shifted distribution function due to the plasma current density j_e or toroidal rotation velocity v_{tr} will be discussed separately. For the hot ions we shall assume the classical distribution [22]

$$f_h(v)=\begin{cases}\dfrac{1}{4\pi}\dfrac{\tau S}{v^3+v_c^3} & \text{for } v<v_b \\ 0 & \text{for } v>v_b\end{cases} \tag{4}$$

$$v_b=\left(2E_b/m_i\right)^{1/2} ,$$

$$S=\frac{Hf\cdot P_b}{E_b V_p} ,$$

$$\tau^{-1}=\frac{8}{3}\left(\pi m_e/2\right)^{1/2}\frac{e^4 n_e \Lambda_1(T_e,n_e,Z_{eff})}{m_i T_e^{3/2}} ,$$

$$\Lambda_1(T_e,n_e,Z_{eff})=\ln\left(\frac{3T_e^{3/2}}{2Z_{eff}^2 e^3 \pi^{1/2} n_e^{1/2}}\right) ,$$

$$v_c=\left[(3/4)\left(\pi m_i/m_e\right)^{1/2} Z_{eff}\right]^{1/3}\left(2T_e/m_i\right)^{1/2} .$$

where Λ_1 is the Coulomb logarithm, V_p is the plasma volume, Hf is a factor of the NBI power distribution in volume assumed equal to unity in our analysis.

The main processes and phenomena that determine the pellet ablation are illustrated by Fig. 1. As an example, a real cloud near the ablating pellet the image obtained using high speed photography with exposure time equal to 5×10^{-6} s is shown upward the scheme (T-10 tokamak, hydrogen pellet, r_{po}=0.067 cm, $v_p=6\times10^4$ cm/s, $B=2.3\times10^4$ G, T_e=500 eV, $n_e=2\times10^{13}$ cm^{-3}). The main ablating heat flux is dominated by the thermal electrons. As the

magnetic field is strong and radius of gyration for the electrons is much less than the pellet radius they can move to the pellet surface only along the magnetic field lines. This flux is one dimensional and at infinity it is equal to [1]

$$Q_{eo} = \left(1/4\right)\left(8T_e/\pi m_e\right)^{1/2} 2T_e \qquad (5)$$

As the plasma minor radius a is usually substantially greater than the pellet radius the density of this heat flux is homogeneous across the ablating channel. Before this flux has reached the pellet surface, it is modified significantly in the following processes.

First, it should penetrate through the double layer between the hot ambient plasma and cold plasma of the cloud flowing away from the pellet surface in the toroidal direction or in the sheath near the ionization radius. The value of the potential drop in the double layer has been estimated in the case of hydrogen plasma by Rozhansky [12]

$$e\Delta\phi = (1.8-2)T_e \qquad (6)$$

The potential drop in the sheath is of the same order [4]. Penetration through the double layer or the sheath doesn't change the distribution function of the electrons in the velocity space but decreases the effective concentration n_e in the particle flux by a factor of $\exp(-e\Delta\phi/T_e)$. After the double layer the electron heat flux Q_{e1} will be ~7 times less than Q_{eo}

$$Q_{e1} = \left(1/4\right)\left(8T_e/\pi m_e\right)^{1/2} 2T_e \exp\left(-e\Delta\phi/T_e\right) \qquad (7)$$

This phenomenon may be included into the ablation analysis later.

Let us now assume that $\Delta\phi$=0. Then the flux modification is determined by energy losses due to inelastic scattering on the cold fully ionized plasma, partially ionized plasma and the neutral cloud. As it was shown in Reference 5, the elastic scattering usually taken into account [1-3, 6, 10] is not significant for the electron heat flux decelerating process. So here we shall consider only inelastic scattering with the loss-function in a form [6] :

$$L_e(E) = \left(2.35\cdot 10^{14} + 4\times 10^{11} E\right)^{-1} \quad \text{eV cm}^2 \qquad (8)$$

This loss-function may be used in all the three slowing down regions as neutral, partially ionized and fully ionized plasma.

Transition between the neutral cloud and the fully ionized cold plasma is determined by the ionization length r_i as well as by the ionization and recombination balance. We shall not discuss the

problem of this transition but note that experimentally the transverse scale of the partially ionized zone is less than 1 cm and the longitudinal length is of the order of several cm's (see Fig. 1). In any case, these scales are much greater than the decay length of the neutral density which is less than the pellet radius [2].

The electron energy losses along the pass of the trajectory h are determined by equation

$$dE/dh = -L_e(E)(n_a + n_i) = -F \quad . \tag{9}$$

It is known [23] that modification of the distribution function in presence of a force acting against the velocity direction is determined by the equation

$$v\frac{\partial f_e}{\partial h} - \frac{1}{m_e v}\frac{\partial}{\partial v}(vFf_e) = 0, \qquad h = x/\varsigma \ , \qquad \varsigma = \cos\theta \tag{10}$$

where θ is the pitch angle. In our assumptions that the angle scattering is not significant two last equations are valid.

The solution of this equation is

$$f_e(E,\varsigma) = \left(E_{eo}(Sn,E,\varsigma)/E\right)^{1/2} n_e \exp\left(-E_{eo}(Sn,E,\varsigma)/T_e\right)\left(L_e\left(E_{eo}(Sn,E,\varsigma)\right)/L_e(E)\right) \tag{11}$$

The energy flux density onto the pellet surface is

$$Q_e(Sn) = \frac{4\pi}{m_e^{1/2}(2\pi T_e)^{3/2}} \int_0^1 \varsigma d\varsigma \int_0^\infty E^2 f_e(E,\varsigma) dE \tag{12}$$

The energy modification may be obtained from Eqs. (8),(9) analytically

$$E_{eo} = -587.5 + \left[587.5^2 + 5\times10^{-12}\left(Sn\varsigma^{-1} + 2.35\times10^{14}E + 2\times10^{11}E^2\right)\right]^{1/2} \tag{13}$$

where

$$Sn = \int_{r_p}^\infty (n_a + n_i)\, dx \tag{14}$$

is the optical length of the cloud along the magnetic field. Changes of the heat flux depend only on the

integral Sn and do not depend on the distribution of the losses along the trajectory. A dependence of the heat flux on Sn for a plasma parameters T_e=T_i=500 eV, n_e=10^{13} cm^{-3}(typical for contemporary experiments) is shown in Fig. 2. It is seen that the heat flux decreases almost exponentially with growth of the optical length. We should emphasize two differences of our approach [5] and the multienergy one [6,10]. Although in References 6,10 several energy groups were used for the energy flux calculations a correct analysis of the distribution with different angles was not fulfilled. Also, the approach corresponds to the assumption ζ =1 in the equation for energy (13). Such a simplification gives significant increase of the heat flux, especially in the region with high flux deceleration. The effect that may be seen from a comparison of the curves 1 and 2 in Fig. 2 is growing with the optical length and reaches 3-5 in the practically interesting region of the flux deceleration (>100).

Another significant difference (see Fig. 2 and compare with Fig. 7 in Reference 6) is that we have no stopping energy for electrons. Appearance of this energy [6] is likely resulting from the limited amount of energy groups used in the computer calculations.

Once the problem of the energy flux modification is solved [5], we should discuss the model for the optical length of the cloud.

This problem for the neutral cloud was solved numerically [5]. The erosion speed of a hydrogen surface dr_{pe}/dt with the curvature radius r_p under the radial heat flux Q_{eo} may be approximated by the expression [2]

$$dr_{pe}/dt = -1.25\left(Sn/2r_p n_m\right)\left[\frac{(Q_{eo}-Q_e)r_p(\gamma-1)}{4m_i Sn}\right]^{1/3} \qquad (15)$$

where n_m is the molecular density of solid hydrogen (2.63×10^{22} cm^{-3}), m_i is the hydrogen atom mass (1.67×10^{-24} g), γ = 7/5 is the ratio of specific heats for hydrogen gas. This equation relates the erosion energy flux and the optical length of the neutral cloud.

The problem of the plasma optical length that has been discussed intensively during last years [4-8,13-15] looks at first view very complicated. Such a complicity arises from classical (collisional transport) approach to the problem. The time for the plasma shift from the ablating channel has been analyzed by several authors. The magnitude was estimated as r_i/v_p [6,13], $(r_i/c_s)(R/2r_i)^{1/2}$ [14] (here c_s is the ion sound velocity in the cloud and R is the major radius of a machine), or $\{r_i/(v_p^2+v_{pol}^2)^{1/2}\}(<V_{tor}>/v_{AC})(<n_i>/n_i)^{1/2}$ [15] (here v_{pol} is the poloidal drift velocity, V_{tor} is the longitudinal plasma expansion speed, v_{AC} is the Alfven velocity inside the cloud, $<n_i>$ is the ion density averaged over the cloud). These considerations predict significant optical length of the plasma cloud. However, they do not take into account the instability that develops in the partially ionized plasma near the pellet. This instability is very strong and the striations moving across the magnetic field have been observed in many experiments [24,25]. The typical drift velocity of the striations lies

in a range of (3-5)$\times 10^6$ cm/s and may be roughly estimated as

$$v_{str} = {cT_e}/{er_i B} \quad , \qquad {r_i}/{v_{str}} = {eBr_i^2}/{cT_e} \tag{16}$$

This velocity is greater than the previous estimations performed on base of the poloidal rotation velocity (r_i/v_{pol} [4,5]) that have shown insignificant plasma optical length. So, we conclude that it is not necessary to take plasma shielding into account except very special conditions, when the cloud is stable.

Ignoring plasma shielding, it is possible to obtain the erosion rate near the axis (the angle α between the radius-vector and the magnetic field is 0) of the electron ablating channel. At this point the conditions correspond exactly to the assumptions used in derivations of the hydrodynamic scaling Eq. (15). We should exclude Sn from the Eqs. (12) and (15) for the heat flux density and erosion rate, keeping in mind that the energy balance between sublimation energy flux and electron heat flux Q_e on the pellet surface is valid.

$$-\lambda_m n_m \, {dr_p}/{dt} = Q_e(Sn) \tag{17}$$

Here λ_m =10.7 meV/mol is the molecular sublimation energy for hydrogen. This equation may be solved graphically by plotting the erosion energy flux in Fig. 2 (see curve 7). The stationary conditions correspond to the cross of the lines 1 and 7 at Sn=1.95$\times 10^{18}$ cm^{-2} giving the energy flux density onto the pellet surface 8.22$\times 10^{10}$ erg/(cm^{2}s) or ablation rate density equal to 9.56$\times 10^{24}$ atom/(cm^{2}s). At the same conditions the Parks scaling Eq. (1) gives the ablation rate density averaged over the pellet surface

$$\left({1}/{4\pi r_p^2}\right) {dN}/{dt} = 8.9\times 10^{14}\, n_e^{0.333} T_e^{1.64} r_p^{-0.667} M_i^{-0.333} \tag{18}$$

The scaling laws for ablation with Maxwellian distribution of the electrons and monoenergetic one are close [5]. So we can normalize the ablation rate flux density and use the expression for the axis point in the form

$$ {dr_{peo}}/{dt} = -1.18\times 10^{15}\, n_m^{-1} n_e^{0.333} T_e^{1.64} r_p^{-0.667} M_i^{-0.333} \tag{19}$$

Our erosion rate is 2.65 times larger than the Parks scaling predicts.

Let us consider the ablation problem if the α-value differs from zero. The heat flux density onto the pellet decreases as $Q_e \cos\alpha$ [4,5]. This effect is significant for the pellet shape modification

during ablation and for development of the general algorithm of the penetration analysis. Usually used one dimensional approach [6] should be modified for the case of the pure electron ablation. Analysis of the impurity pellet ablation [11] has shown that the significant parameter for ablation is not the current pellet radius r_p related with the pellet volume (assumed to be sphere during ablation) but the initial pellet radius r_{po}. This effect was numerically seen and briefly discussed in Reference 5. Here we will show that similar to the impurity pellet the initial pellet radius is significant for the hydrogen pellet as well. This mode of ablation is mentioned as "lentil" below because the pellet has a form of the spherical lens resembling a lentil.

In Fig. 3 situation with the heat flux propagation and the gas flow expansion at the point $\alpha \neq 0$ is shown schematically. As the neutral cloud optical length is forming at a scale less than the pellet radius let us consider the problem as almost flat. The total amount of energy that longitudinal heat flux supplies to the cloud is the same as in the case of radial flux with lower density

$$Q_{eo}(\alpha) = Q_{eo}(Sn)\cos\alpha \tag{20}$$

We note that the hydrodynamic scaling Eq. (15) is invariant relative to transformations

$$Q_{eo}(\alpha) = Q_{eo}(Sn)\cos\alpha\ ,\ \ Sn(\alpha) = Sn\cos\alpha\ ,\ \ {dr_p(\alpha)}/{dt} = \left({dr_p}/{dt}\right)\cos\alpha \tag{21}$$

Thus, for this distribution the erosion rate in the magnetic field direction is constant

$${dx_p}/{dt} = \left({1}/{\cos\alpha}\right){dr_p(\alpha)}/{dt} = Const(\alpha) \tag{22}$$

as well as the optical length $Sn_x(\alpha)$ along the magnetic field line

$$Sn_x(\alpha) = {Sn(\alpha)}/{\cos\alpha} = Const(\alpha) \tag{23}$$

Assuming these conditions at every point of the pellet surface, the curvature of the surface is constant during ablation and the ablation rate at any moment can be obtained using the equation

$${dN}/{dt} = -4\pi n_m\left({dr_{peo}}/{dt}\right)\left\{r_{po}^2 - \left[\frac{1}{v_p}\int_r^a\left({dr_{peo}\left(n_e, T_e, r_{po}\right)}/{dt}\right)dr'\right]^2\right\} \tag{24}$$

(a is the limiter radius corresponding to the plasma boundary.)

The expression for the erosion speed dr_{peo}/dt should be calculated using Eqs. (19) at the fixed initial radius r_{po} while the plasma parameters are to be taken along the pellet trajectory.

It is clearly seen from Eq. (19) that the erosion rate increases for smaller radii or higher curvature of the pellet surface. For the initially non spherical pellet that means the parts with a higher curvature should ablate faster and a tendency for formation of the pellet surface with the fixed curvature may be expected. So, we can conclude that initially cylindrical pellet (r_{po}x2r_{po}) will form a sphere of the radius of r_{po} soon after the beginning of ablation.

The pellet ablation rate calculated on base of the algorithm described with the parameters of the pellet and plasma: r_{po}=0.075 cm, v_p=6.6×10^4 cm/s, a =32 cm,

$$T_e(r)=1000\left[1-\left(r/a\right)^2\right]^2 \text{ eV}, \quad n_e(r)=4\times10^{13}\left[1-\left(r/a\right)^2\right] \text{ cm}^{-3} \quad \cdot \quad (25)$$

is shown in Fig. 4. For a comparison the standard calculations on base of the one dimensional spherical ablation using Eq. (1) are presented as well. The penetration lengths for both cases differ on ~20% and the ablating profiles for the models are different. For the lentil approach the ablation rate at the final stage is higher. That mode of the ablation rate better correlates with the H_α measurements.

1.3. Ion ablation

Although the ion heat flux is significantly less than the electron one the ablation may be sensitive to it in two-dimensional case. The ion flux may be considered to be isotropic as against the electron heat flux. However, the problem for ions remains two-dimensional. As it is seen from Fig. 1 the zones of the pellet poles are not screened by the electron ablated cloud and we should find the energy ablation balance for the ions at $\alpha=\pi/2$ similar to Eq. (17) separately. The optical thickness of the cloud increases due to electron ablation for the smaller α. In this region the ion penetration should be analyzed together with the effects of electron ablation.

The situation near the poles looks like as follows. Analysis is similar to the electron case but a different loss-function for ions should be used [20]

$$L_i(E)=1.93\times10^{-16}E^{0.4} \qquad \text{eVcm}^2 \qquad . \qquad (26)$$

Energy transformation inside the cloud is then determined by

$$E_o(E,\varsigma)=\left(E^{0.6}+1.16\times10^{-16}Sn\varsigma^{-1}\right)^{1.667} \qquad (27)$$

and energy flux is

$$Q_i(Sn)=\frac{4\pi}{m_i^{1/2}(2\pi T_i)^{3/2}}\int_0^1 \varsigma d\varsigma \int_0^\infty E^2 f_i(E,\varsigma)dE \quad , \tag{28}$$

where

$$f_i(E,\varsigma)=\left(E_o(E,\varsigma)/E\right)^{1/2} n_i \exp\left(-E_o(E,\varsigma)/T_i\right)\left(L_i(E_o(E,\varsigma))/L_i(E)\right) \quad .$$

Dependence of the ion heat flux on the cloud optical length is shown in Fig. 2. Here we also should note the difference in the flux deceleration for the ions with different pitch angles. The various pitch angles of ions correspond to angles between the normal to the pellet surface and the velocity vector. (This effect is shadowed for electrons by the magnetic field.)The corresponding equation for the erosion speed has the form

$$dr_{pi}/dt=-1.25\left(Sn/2r_p n_m\right)\left[\frac{(Q_{io}-Q_i)r_p(\gamma-1)}{4m_i Sn}\right]^{1/3} \tag{29}$$

The balance is reached at $Sn=4.25\times10^{17}$ cm^2 and energy flux density onto the pellet surface equal to 8.53×10^9 erg/(cm^{2}s) which value is 10 times less than in the electron case. Nevertheless, the ion ablation is much higher than is expected in one-dimensional approach.

If the NBI is used on a machine, the ion part may be much larger. Outside the cloud (for the heat flux of hot ions with the distribution function determined by Eq.(4)) we have

$$Q_{ho}=\frac{1}{12}m_i\tau S\left\{v_b^3-v_c^3\ln\left[1+\left(v_b/v_c\right)^3\right]\right\} \tag{30}$$

and on the pellet surface

$$Q_h(Sn)=\frac{4\pi}{m_i^{1/2}(2\pi T_i)^{3/2}}\int_0^1 \varsigma d\varsigma \int_0^{E_m} E^2 f_h(E,\varsigma)dE \tag{31}$$

where

$$f_h(E,\varsigma)=\left(E_o(E,\varsigma)/E\right)^{1/2}\left[L_i(E_o(E,\varsigma))/L_i(E)\right]n_h\left(m_i/2\right)^{3/2}\left(E_o(E,\varsigma)^{3/2}+E_c^{3/2}\right)^{-1}$$

$$E_m(Sn,\varsigma)=\left(E_b^{0.6}-1.16\times10^{-16}Sn\varsigma^{-1}\right)^{1.667} \quad .$$

The hot ion heat flux is also sensitive to the pitch angle (compare curves 5 and 6 in Fig. 2). The main difference of the hot ion flux and the heat ion flux is a limit after which the fast ions are stopped in the cloud. In the case presented in Fig. 2 it is reached at $Sn = 3.7 \times 10^{18}$ cm^{-2}.

1.4. General case

In general case where all the fluxes are taken into account simultaneously the erosion rate has the form

$$dr_p(\alpha,\beta)/dt = -1.25\left(Sn/2\rho_p n_m\right)\left[\frac{(Q_{eo}\cos\alpha + Q_{io} + Q_{ho})\rho_p(\gamma-1)}{4m_i Sn}\right]^{1/3} \quad (32)$$

where the $\rho_p(\alpha,\beta)$ may be interpreted as the average two-dimensional inverse curvature $<s>$ of the pellet surface at the point (r_p,α,β) on the pellet surface

$$\rho_p = <s>^{-1}, \qquad <s> = \left(s_\alpha + s_\beta\right)/2, \qquad s_{\alpha,\beta} = d^2/dl^2_{\alpha,\beta}\, r_p(\alpha,\beta) \quad (33)$$

Here $l\alpha$, $l\beta$ are the paths in α-angle and β-angle directions along the pellet surface. Of course, it is better to combine in more rigorous approach the results for the spherical and cylindrical gas expansion. However, this definition is not very significant because in the case of cylindrical pellet the curvature will differ from r_{po}^{-1} only before one third of the pellet volume is ablated. The total flux Q_s in the direction of the pellet surface determined by the Eqs. (12), (28), (31)

$$Q_s = Q_e\cos\alpha + Q_i + Q_h \quad (34)$$

together with Eqs. (32), (33) should be used for determination of the local optical length $Sn(\alpha,\beta)$. And ablation rate may be calculated by the integral

$$dN(r)/dt = 2n_m \int_0^{2\pi}\int_0^{\pi} dr_p(\alpha,\beta,r)/dt\left[r_{po}(\alpha,\beta) - \frac{1}{v_p}\int_r^a dr_p(\alpha,\beta,r')/dt\, dr'\right]^2 \sin\alpha\, d\alpha\, d\beta \quad (35)$$

As the pellet curvature tends to be minimal in average at the last stage of ablation the pellet form will be of "lentil" type for an arbitrary initial form.

1.5. Electrostatic shielding effects

The problem of electrostatic shielding of the pellet surface during ablation had been discussed even in the first analysis by Spitzer [26]. There the ablating pellet was considered as an electrostatic probe under the floating potential $\Delta\phi$. More detailed similar analysis [4] of this effect on base of the refined theory of Laframboise [27] has shown that in the typical tokamak conditions with an assumption of $T_i=T_e$ the floating potential $\Delta\phi$ of the spherical probe with $\rho_i>r_i>>\rho_e$ (here ρ_i and ρ_e are the gyroradii of the ions and electrons) will be close to $1.7T_e/e$. The corresponding electron and ion heat fluxes at the cloud boundary integrated over the pellet surface will be as follows:

$$q_e = 2(2\pi)^{1/2} n_e T_e^{3/2} r_p^2 m_e^{-1/2} \exp(-e\Delta\phi/T_e) \tag{36}$$

$$q_i = 2(2\pi)^{1/2} n_e T_e^{1/2} r_p^2 m_i^{-1/2} f(T_i/T_e, \xi, \Delta\phi)(2T_i + e\Delta\phi) \tag{37}$$

$$\Delta\phi = -\frac{T_e}{e}\ln\left(\frac{2m_e^{1/2} f(T_i/T_e, \xi, \Delta\phi)}{m_i^{1/2}}\right) \tag{38}$$

$$\xi = r_p(4\pi n_e e^2/T_e)^{1/2} = r_p/r_d \tag{39}$$

where r_d is the Debye length and the function f was tabulated [27]. Note that more available results [28] for the ion temperature $T_i=0.1T_e$ give the floating potential close to the presented one ($\Delta\phi=2T_e/e$).The total heat flux of the electrons and ions onto the pellet surface under the floating potential is then equal to

$$q_s = 2(2\pi)^{1/2} n_e T_e^{1/2} r_p^2 m_e^{-1/2} \exp(-e\Delta\phi/T_e)(T_e + 2T_i + e\Delta\phi) \tag{40}$$

The first term in the brackets (T_e) corresponds to the electron heat flux and the other two belong to the ion part. This part, when the pellet cloud charges, becomes significantly larger than the electron part. This phenomenon is explained by absolutely different mechanism of the ion flux formation. Unlike the electron heat flux directed along the magnetic field lines, the ion heat flux is formed in the sheath near the cloud surface. The size of this region is of order the pellet radius. The ions are accelerated in this sheath additionally by the potential $e\Delta\phi$ and reach the boundary of the cloud with average energy of $2T_i+e\Delta\phi$. In comparison with the direct ion heat flux Q_{io} the increase as large as 7 times occurs

$$\frac{1}{2}(m_i/m_e)^{1/2}\exp(-e\Delta\phi/T_e)(1+e\Delta\phi/2T_i)=7.17 \qquad (41)$$

As a result the total heat flux coming onto the cloud surface is only two times less than the electron heat flux Q_{eo} integrated over the ablating channel.

Therefore, the influence of the charging is not very large (effect on the heat fluxes is of order 2). However, the structure of the heat fluxes is drastically changed. Instead of the longitudinal electron heat flux almost radial ablating heat flux is transferred by the ions.

We should note that one-dimensional analysis of the problem without taking into account ion currents [12] has a small projection onto a pellet ablation in the tokamak/stellarator experiments. Transverse ion current to the cold plasma region near the pellet at the potential drop [12] should be so large that it cannot be neglected in the electron current density balance.

For a correct determination of the pellet cloud potential more effects, especially influence of the partially ionized plasma on the charging, should be considered. However, in any case the pellet potential may be only lower than the floating potential. If we assume that this voltage drop is located at the cloud boundary and has the same symmetry as the cloud (this assumption is based on the high conductivity of the plasma in this zone) we can obtain the pellet ablation rate in two-dimensional approach as earlier.

For the electron heat flux density we can use Eq. (7). For the ion heat flux it is difficult to calculate rigorously the distribution function and penetration through the cloud. However, as an estimation from the low-value side we can use the penetration dependence of the ion heat flux shown in Fig. 2. Then the total heat flux density onto the pellet surface Q_S is

$$Q_s(Sn,\alpha)=Q_e(Sn)\exp(-e\Delta\phi/T_e)\cos\alpha + \frac{1}{2}Q_i(Sn)\,Q_{eo}/Q_{io}\exp(-e\Delta\phi/T_e)(1+e\Delta\phi/2T_e) \qquad (42)$$

For the conditions of the Fig. 2 the dependencies of the heat flux versus the optical length Sn are shown in Fig. 5 (a, b, c) for the $\alpha=0,\pi/4$ and $\pi/2$. At the axis of the electron ablating channel ($\alpha = 0$) the value of the cloud optical length is decreased to 1.32×10^{18} cm^{-2} from 1.95×10^{18} cm^{-2} without shielding. It is seen that only the electrons are penetrating to the pellet surface here. A weak influence of the ions increasing the ablation rate density with decrease of the optical length is seen as well. Even at the region with $\alpha=\pi/4$ the ion flux influence on the ablation is weak (see Fig. 5 (b)). Only near the poles ($\alpha>3\pi/8$) the ion ablation becomes significant and comparable with the electron part (Fig. 5 (c)). The optical length of the cloud at the poles is equal to 5.1×10^{17} cm^{-2}.

The dependencies of the ablation rate density on the poloidal angle α are presented in

Fig. 6 (a). In the case of charged pellet the distribution over the pellet surface is much more homogeneous and the ablation rate densities at $\alpha > 3\pi/8$ where a significant part of the pellet area is located are much higher than in the $\Delta\phi=0$ case. The angular dependencies of the ablation density ($Q_S \sin\alpha$ and $Q_e \cos\alpha \sin\alpha$) are shown in Fig. 6 (b). The integrals under the curves 1 and 2 proportional to the total ablation rate dN/dt are equal to
9.88×10^{10} and 8.47×10^{10} for the cases without and with the pellet changing correspondingly. Little difference in the gross ablation rates is expected between the charged and not charged pellet. But, the distribution of the ablation rate density over the pellet surface is substantially different from each other. A possible phenomenon, which is sensitive to this changing of symmetry, is the pellet trajectory deflection due to current in the plasma. If the ion flux has spherical symmetry and only the asymmetric electron flux creates the toroidal acceleration, then the significant difference of this flux may be observed from the analysis of the pellet deflection. This effect is analyzed in the next section.

1.6. Hydrogen pellet trajectory in a plasma with current

Along with investigations of the ablation rate more fine effects were observed during ablation. They are changes of the ablation rate near the rational magnetic surfaces [29], cloud instabilities [24] and toroidal deflection of the pellet trajectory in a plasma with current [11]. The last phenomenon is well known on tokamaks experimentally [30]. For the case of the carbon or lithium pellet a model describing the pellet ablation and trajectory has been developed [11].

In this paper a model for the hydrogen pellet acceleration in a plasma with current is described. The main difference between the hydrogen pellet and the impurity pellet is in the structure of the clouds. In the case of hydrogen only a small part of the heat flux reaches the pellet surface while in the impurity case the cloud is almost transparent for the electrons. We shall analyze two possible cases of ablation with the spherical and the spherical lens symmetry of the pellet during ablation. The model is compared with the results of T-10 tokamak.

.

1.6.1. Model Description

Let us assume that fully ionized background plasma has the Maxwellian distribution function

$$f(n_e, \mathbf{v_e}, T_e) = n_e \left(m_e / 2\pi T_e\right)^{3/2} \exp\left[-m_e(\mathbf{v_e} - \mathbf{u})^2 / 2T_e\right] \qquad (43)$$

with a temperature T_e, density n_e and current density

$$j_e = e n_e u \qquad (44)$$

Here m_e and v_e are the mass and the thermal velocity of electrons, u is the drift velocity. For such a plasma the additional heat flux exists in the counter-current direction which value may be estimated as [31]:

$$Q_{add} = (5/2 + F(z_{eff}))n_e T_e u \tag{45}$$

Function $F(z_{eff})$ is a weak function of the plasma effective charge. This function is equal to 0.9 at z_{eff}=2. The additional heat flux increases ablation rate at the counter-current side and the reactive force causes the pellet acceleration in toroidal direction. Analyzing the acceleration process one should solve the problem of this flux modification inside the ablating cloud near the pellet. Here, in the neutral shielding regime the problem can be solved without detailed analysis of these modifications. Let us assume first that the pellet is spherical and the pellet ablation rate is given by the neutral gas shielding model:

$$dN/dt = 1.12\times10^{16} n_e^{0.333} T_e^{1.64} r_p^{1.333} M_i^{-0.333}$$

Toroidal pellet acceleration is determined by the rocket equation:

$$M(t)(dv_z/dt) = aUm_i DN(t) \tag{46}$$

where $M(t)$ is the pellet mass, v_z is the toroidal velocity, a=<cos$^2\theta$>=1/2 is the factor that accounts averaging the ablation force over the spherical pellet surface, U is the hydrogen atoms' velocity near the pellet surface, and $DN(t)$ is the additional particle loss due to the current in plasma.
As we have assumed the spherical form of the pellet during ablation then:

$$M(t) = (4/3)\pi r_p^3(t) m_i n_a \tag{47}$$

n_a=5.26×10^{22} cm^{-3} is the atomic density for hydrogen, m_i=1.67×10^{-24} g is the hydrogen mass.
The value of U may be determined as the gas flux velocity at the sonic radius in Parks model [3]

$$U = v^* = 86.6 r_p^{1/3} n_e^{1/3} T_e^{-0.07} \tag{48}$$

The value of U is of order 5×10^5 cm/s.
For an estimation of $DN(t)$, we have assumed that the additional heat flux existing at the infinity is modified in the same manner as the main one responsible for the ablation. Since the plasma temperature at the infinity is not changed, the distribution function is modified by a change of electron

density, or the additional heat flux determined by Eq. (45) is taken into account as the density increase from the counter-current side and the density decrease from the co-current side. Then combining the Eqs. (44)-(47) we obtain

$$Dn_e = (5/2 + F(z_{eff}))j_e / (ev_{Te}),\ v_{Te} = (2T_e / m_e)^{1/2} \tag{49}$$

$$DN = \partial / \partial n_e (dN / dt) Dn_e \tag{50}$$

Finally, for the acceleration we have

$$dv_z / dt = 5.94 \times 10^{14} U n_a^{-1} n_e^{-0.667} T_e^{1.64} r_p^{-1.667} M_i^{-0.333} Dn_e \tag{51}$$

The modified distribution function is shown in Fig. 7. The line 1 is the non shifted Maxwellian distribution, the line 2 is the shifted one due to the current and the line 3 is the distribution function used in the model. The ratio u/v_{Te} = .1 is used for this plot. It is seen that in small energy region our distribution function differs from the shifted Maxwellian function. However, it is not significant for the problem because in the u/v_{Te} >1.5 region our distribution and the shifted Maxwellian one are the same. As we have seen in sections 1.1 and 1.2 this region does determine the power balance of the ablation.

For the case of the lentil type ablation the set of the equations describing the pellet acceleration will be as follows:

$$dv_z/dt = a(r)U(r)DN(r)/V_n(r) \tag{52}$$

$$a(r) = \frac{2}{3}\left[1 + \left(\frac{1}{v_p r_{po}} \int_r^a \frac{d}{dt} r_{peo}(r_1) dr_1\right)^3\right] \tag{53}$$

$$U(r) = 86.6 r_{po}^{1/3} n_e(r)^{1/3} T_e(r)^{-0.07} \tag{54}$$

$$DN(r) = 2.796 \times 10^{15} n_e(r)^{-0.667} T_e(r)^{1.64} r_{po}^{1.333} M_i^{-0.333} Dn_e(r) \tag{55}$$

$$V_n(r) = \frac{4}{3}\pi r_{po}^3 2n_m - \frac{1}{v_p} \int_r^a \frac{dN}{dt}(n_e(r_1), T_e(r_1), r_{po}) dr_1 \tag{56}$$

Here dN/dt and D_{ne} is determined by Eqs. (24) and (49), respectively.

In the case of charged pellet the electron heat flux is significantly suppressed. However, the ablation rate does not change significantly. Ablation is close to the spherical version. For determination of the pellet trajectory one should use the set of Eqs. (46)-(51) with the following modifications. The ablation rate dN/dt is less than the lentil ablation by the factor of 0.856 when the decrease of the ablation rate due to the pellet charging in the case of the Maxwellian electrons and significant ion ablation is taken into account (see section 1.6)

$$dN / dt = 1.27 \times 10^{16} n_e^{0.333} T_e^{1.64} r_p^{1.333} M_i^{-0.333} \tag{57}$$

and Eq. (51) should be multiplied by $1.33 \cdot \exp(-e\Delta\phi/3T_e)$

$$dv_z / dt = 5.94 \times 10^{14} U n_a^{-1} n_e^{0.667} T_e^{1.64} r_p^{-1.667} M_i^{-0.333} D n_e \times 1.33 \exp\left(-e\Delta\phi / 3T_e\right) \tag{58}$$

This is an approximate estimation. In more rigorous approach one should use the entire procedure of determining the heat flux balance described in section 1.6.

Influence of the neutral beam on the acceleration of the pellet may be considered as follows. The volume power of the beam is on the order of 1 W/cm^3 and the energy flux density $Q_{hb} = \left(2/m_i\right)^{1/2} n_b E_b^{3/2}$ may be expected as large as 10^{10} erg/cm^{2}s. This heat flux is too small to affect the pellet ablation or acceleration. Nevertheless, if the NBI is performed from one direction the toroidal rotation of the plasma may occur. The magnitude of the v_{tr} is of order 10^7 cm/s or higher. The additional heat flux Q_{tr} associated with this toroidal plasma rotation may be estimated as

$$Q_{tr} = \frac{3}{2} v_{tr} n \left(T_e + T_i\right) \tag{59}$$

For n_e=10^{13} cm^{-3}, v_{tr}=10^7 cm/s and T_e=T_i=500 eV this flux is equal to 2.5×10^{11} erg/cm^{2}s. This value is only 25 times less than the thermal electron heat flux. However, the flux is directed almost along the magnetic field lines, so a substantial screening of this flux in the neutral cloud will take place. It participates in the heating of the cloud and should be added to the fluxes in Eq. (32). But, in the balance on the pellet surface (Eq. (34)) it can be neglected obviously. This flux does not affect the total ablation rate and creates negligible acceleration.

1.6.2. Simulation results

The model for the pellet deflection was used for simulation of the hydrogen pellet trajectory in T-10 tokamak. The parameters of the simulation and the profiles versus minor radius r were as follows:

$n_e(r) = 3\times10^{13}\ (1-(r/a)^2)$ (cm^{-3})

$T_e(r) = 1200\ (1-(r/a)^2)^2$ (eV)

$j_e(r) = 300\ (1-(r/a)^2)^3$ (A/cm^2)

$z_{eff} = 2$, $F(z_{eff}) = 0.9$, limiter radius a =32 cm

The density shift Dn_e of order 10% is necessary in central region of the plasma. For the hydrogen pellet with the radius r_p =0.075 cm and velocity v_p =6.6×10^4 cm/s the trajectory parameters (acceleration, velocity, track) are presented in Fig. 8. Ablation rate with the trajectory parameters in the case of charged pellet is presented in Fig 9. The curves marked 1 are calculated in an assumption of the lentil mode of ablation, while the mark 2 corresponds to the spherical ablation without charging and the mark 3 shows the calculations in the case of charged pellet. The maximum magnitude of acceleration of 3×10^9 cm/s^2 is predicted. Toroidal pellet velocity grows up to ~1000 m/s and the deflection is equal to ~5 cm. The largest acceleration and deflection are foreseen for the spherical electron ablation in accordance with the Parks scaling. The lowest one is expected in the case of the charged pellet. However, the difference between the options considered above is not very large and will not be distinguished in experiments.

1.6.3. Discussion

The proposed model predicts the hydrogen pellet acceleration proportional to the plasma current. This is valid also for impurity pellets. Absolute values of the deflection for the carbon pellet are approximately the same in the T-10 tokamak [11]. This prediction is verified by the T-10 experiment where several cm displacements for the carbon pellets were typical and displacements of hydrogen pellets were of order of several cm as well.

High acceleration for the hydrogen pellet is determined by several reasons. The pellet has low density and relatively low mass (this is favorable for the acceleration). The surface velocity U for hydrogen is higher (5×10^5 cm/s) than for carbon (2.4×10^5 cm/s) as well. However, only 1/3-degree dependence on the plasma density is characteristic for the hydrogen instead of linear dependence for the carbon. Deeper penetration length for carbon pellet allows it to reach the same displacement at lower acceleration.

In the case of non-Maxwellian plasma the effect can be estimated as well but the whole procedure of the distribution function modification in the cloud should be considered. This phenomenon is briefly discussed in the next issue.

1.6.4. Conclusions

A model for a hydrogen pellet acceleration in toroidal direction during ablation is developed. The model predicts the acceleration proportional to the plasma current density as in the case of the impurity pellets. Typical acceleration values in a middle size tokamak can reach 10^9 cm/s^2 and the deflection value of 3-4 cm, close to the carbon pellet's deflection in the same plasma, is expected in spite of shorter penetration length.

1.7. Hot electrons influence on a pellet ablation

If the distribution function differs from the Maxwellian type, the pellet ablation may change significantly. This situation might occur during the plasma heating by ECRH or ICRH methods. For the electron energy greater than the critical energy E_{cr} it is possible to apply the procedure described in part 1.2 for finding the heat flux modification and ablation rate .
The optical length of the pellet Sn_p

$$Sn_p = 2n_m r_{po} \tag{60}$$

and the critical penetration energy E_{cr}

$$E_{cr} = -587.5 + (587.5^2 + 5\cdot 10^{-12} Sn_p)^{1/2} \tag{61}$$

as functions of the pellet radius are shown in Fig. 10 (a, b). Electrons with the energies larger than E_{cr} spend only a part of their energy inside the pellet and leave the pellet after penetration. The relative losses of the electron energy inside the pellet $(E_h\text{-}E)/E_h$ are shown as a function of the initial energy E_h in Fig. 10 (c) for the pellet radii changing from 0.02 cm (curve 1) up to r_p=0.2 cm (curve 10). For the typical tokamak conditions the critical energy lies in the range of 150-350 keV. Beyond the critical energy the losses decrease quickly and this phenomenon should be taken into account in the ablation analysis.

The energy losses of the hot electrons are distributed in the pellet volume more or less homogeneously. It is seen from Fig. 11 that represents the energy losses $E_h\text{-}E$ as a function of the pellet radius for several energies in 0.1-1 MeV range.

Penetration of the hot electrons is better near the pellet poles in case of a spherical pellet. The electron energy contributing to the ablation depends on this effect. Effect of the spherical form on energy after penetration through the pellet E is illustrated with Fig. 12 where the $E(\alpha)$-dependencies are shown for the pellets with r_p=0.075 cm and r_p=0.15 cm,

$$E(\alpha) = -587.5 + \left[(E_o + 587.5)^2 - 5\times 10^{12} Sn(r_{po}\cos\alpha)\right]^{1/2} \tag{62}$$

The effect of the pellet form becomes significant near the critical energy E_{cr} and then tends to be of order 2.

Although the energy flux onto the pellet surface

$$Q_{he} = E_h n_h \left(2E_h/m_e\right)^{1/2} \tag{63}$$

rapidly increases with the electron energy E_h, the hot electrons ablating power

$$q_{he} = 2\pi r_{po}^2 n_h \left(2E_h/m_e\right)^{1/2} \int_0^{\pi/2} [E_h - E(\alpha)]\cos\alpha\sin\alpha d\alpha \tag{64}$$

is a weak function of the energy with a maximum near the E_h =200 keV (see Fig. 13). This conclusion is not sensitive to the pellet radius, although the energy losses increase with the pellet radius even faster than the energy flux.

Fraction of energy contributing to ablation versus the initial hot electron energy E_h is shown in Fig. 13 c. It is seen that at higher than the critical energy the electrons penetrate through the pellet with small energy losses, and the ablating power is distributed homogeneously in the pellet volume. The hot electrons will initiate symmetrical ablation or even slightly faster ablation from the opposite to the particle flux side of the pellet. If the energy supplied to the pellet by the hot electrons becomes comparable with the thermal ablating flux, ablation rate balance is governed by the hot electrons while the cloud parameters are still determined by the thermal flux, as seen in Fig. 14. As the hot electron flux is independent of the cloud optical length, it may be assumed constant and should be added to the thermal flux exponentially decreasing with Sn.

Hot electron effective heat flux Q_{he} may be defined as

$$Q_{he} = q_{he}/4\pi r_p^2 \tag{65}$$

In the balance equation

$$-\lambda_m n_m \frac{dr_p}{dt} = Q_e + Q_{he} \tag{66}$$

As seen from Figs. 14 (a) and (b), the cloud optical length and the ablation rate are not changed significantly for the comparable Q_{he} and Q_e. However, if heat flux by hot electrons is two times greater than that of thermal electrons, the contribution from the thermal electron flux is negligible.

Such a behavior of the ablation may be used for the diagnostics of the population of hot electrons. Keeping in mind that the Q_{he} is a weak function of electron energy one can have a good estimation of the hot particles even if the ablation rate is increased less then two times in comparison with the thermal case:

$$n_h \approx 3\times10^{-15}\frac{dN}{dt} \text{ for } r_p = 0.15 \text{ cm and } n_h \approx 4\times10^{-14}\frac{dN}{dt} \text{ for } r_p = 0.075 \text{ cm.}$$

The heat flux Q_{he} may be added to Eq. (34) used for the general ablation analysis

$$Q_s = Q_e \cos\alpha + Q_i + Q_h + Q_{he} \tag{67}$$

Eq. (32) should be unchanged.

The case of the intermediate electron energy $6T_e < E_o < E_{cr}$ is not symmetrical. The ablation rate caused by the hot electrons is greater at the heat flux side, becomes the volume power source is shifted. Under these conditions a large asymmetry in ablation from the flux side and the back side may occur, and this can give rise to a toroidal acceleration of the pellet up to the values much greater than in the thermal case. However, for the estimation the Eqs. (64)-(66) may be applied.

1.8. About one paradox of the one dimensional ablation model

In one dimensional approach to the ablation [6,9] is usual to average the foaling onto the pellet electron heat flux $2\pi r_{po}^2 Q_{eo}$ over the pellet surface $4\pi r_{po}^2$. Then the averaged heat flux $\langle Q_{eo}\rangle = (1/2)Q_{eo}$ is used for the determination of the ablation rate using the hydrodynamic scaling Eq.(15) in accordance to which

$$dr_{po}/dt \sim Q_{eo}^{1/3} .$$

Ablation rate dN/dt is determined by multiplying this erosion speed by the total pellet surface

$$dN/dt \sim 4\pi r_{po}^2 \left(dr_{po}/dt \right).$$

However, this procedure is incorrect. It estimates higher ablation rate substantially because the erosion rate is a very weak function of the heat flux density (1/3-power) while the ablation rate is directly proportional to the pellet surface. As a result the effective ablation rate is artificially increased in $2^{2/3} = 1.59$ times. Much higher ablation rate than that observed in the experiments is obtained in Reference 8 when the Maxwellian distribution is applied to the model. For the case discussed in part 1, for example, the application of the maxwellian distribution increases ablation rate by a factor of 2.65 in comparison with the monoenergetic approach with $E_0 = 2T_e$. Nevertheless in the final result we have erosion speed only 1.33 times higher than in the Parks scaling. It is possible that a drastic disagreement with the Maxwellian ablation noted in Reference 8 might disappear when this effect is taken into account. The effect of plasma shielding will be insignificant as well.

Part 2. Comparison of the theories with the pellet ablation experiments

This part is devoted to a comparison of the models described in part 1 with several ablation experiments. Although pellet ablation is studied for a long time, only a few data can be really compared with theory [5-10,32-34]. This situation is caused by usual lack of information about the plasma or the pellet parameters required for comparison.

There are three types of the data that may be compared with the theories. The most numerous and reliable information is obtained about the penetration length L that is determined by several methods: photo diodes and SXR arrays as well as by the measurements of the pellet velocity or a photography from a perpendicular direction. Second one is the local ablation rate dN/dt that may be obtained studying the H_α or H_β radiation from the pellet by the photo diodes with filters or by the monochromators. The local ablation rate represented by the ablation rate curve is different for the various ablation modes and may be used for distinguishing between the models. This information is also numerous. However, some differences in H_α and H_β signals as well as a deviation of the particle deposition profile obtained by independent methods from these signals [9] suggest necessity of careful analysis of these data. There are also some data on the pellet deflection obtained by the ordinary or CCD-cameras. We consider these results consequently below.

2.1. Penetration length

2.1.1. Accuracy analysis

Trying to distinguish between the theories that give (as we have seen in part 1) close results, it is necessary to define the main parameters of the experiments and the accuracy that allows to make quantitative comparison between the theory and experiment. Let us make this accuracy analysis for the Parks scaling and spherical ablation. For the other models the result will be almost the same.
The penetration length appears at a lower limit after integration of Eq. (1)

$$4\pi \int_0^{r_p} r_p^{2/3} dr_p = \left(1.12\times 10^{-16} / v_p\right) \int_{a-L}^{a} n_e^{0.333} T_e^{1.64} M_i^{-0.333} dr = 4\pi \left(\frac{3}{5}\right) r_{po}^{5/3} \qquad (68)$$

The following parameters are responsible for the penetration depth:
$r_{po} \pm \Delta r_{po}$, $v_p \pm \Delta v_p$, $n_e(r) \pm \Delta n_e(r)$, $T_e(r) \pm \Delta T_e(r)$. The accuracy of the first two characteristics does not change along the trajectory, while the density and temperature accuracy may change substantially. Changing the integral Eq. (68) to a sum we can clearly see the penetration length

$$4\pi\left(\frac{3}{5}\right)r_{po}^{5/3} = 1.12\times10^{-16} M_i^{-0.333} \sum_{j=0}^{k} n_j^{1/3} T_j^{1.64} \frac{L}{k\cdot v_p} \tag{69}$$

If all the parameters are statistically independent we have

$$\left(\frac{\Delta L}{L}\right)^2 = \left(\frac{5}{3}\frac{\Delta r_{po}}{r_{po}}\right)^2 + \left(\frac{\Delta v_p}{v_p}\right)^2 + \frac{\sum_{j=0}^{k} n_j^{0.333} T_j^{1.64}\left[\left(\frac{1}{3}\frac{\Delta n_j}{n_j}\right)^2 + \left(1.64\frac{\Delta T_j}{T_j}\right)^2\right]}{\sum_{j=0}^{k} n_j^{0.333} T_j^{1.64}} \tag{70}$$

The errors of the pellet radius and the electron temperature are most significant for the errors of the penetration length. For the typical experimental conditions ($\Delta r_{po}/r_{po}$ =0.03, $\Delta v_p/v_p$ =0.01, $\Delta n_e/n_e$ =0.1, $\Delta T_e/T_e$ =0.1) one has $\Delta L/L$=0.175. The errors for the plasma parameters are weighted proportionally to the parameter $n_e^{0.333}T_e^{1.64}$ that has the largest contribution at the end of ablation.

2.1.2. Experimental database

Experimental database on the pellet ablation is presented in Table 1 a, b. The data contain both hydrogen and deuterium ablation and cover a region with the r_p = 0.034-0.2 cm, v_p = 42600-140000 cm/s, $n_e(0)$ =(1.25-55)$\times10^{13}$ cm^{-3}, $T_e(0)$ = 780-4490 eV. Typical accuracy for the r_p measurements varies in the range of 0.023-0.05. For the v_p the errors lie in the range from 0.003 (T-10, JET) up to 0.05 (Tore-Supra, Heliotron-E). The density accuracy for all the experiments is 0.1, and for the electron temperature the accuracy of 0.05-0.1 is declared. The penetration depth L has varied in the experiments from 12 cm (Alcator) up to 61 cm (JET). The errors in the plasma and pellet parameters allow to predict the penetration length with the accuracy $\Delta L/L$=0.07-0.15 or ΔL=1-8.2 cm in the absolute values. The main contribution to errors of the penetration length is given by uncertainties on the temperature and the pellet radius. For a comparison with the theories we used the profiles of electron density and temperature that are presented in Table 1 b. Three models were used for the ablation simulation: spherical model based on the Parks scaling, lentil and charged pellet models described in part 1. Here we have calculated ablation without taking into account the ion ablation effects.

Typical penetration, ablation rate and toroidal deflection characteristics are illustrated in Fig. 15. (Tore-Supra #2687-1). The penetration length for the spherical ablation model has the largest value. For

the charged pellet the penetration length is a little bit lower. Lentil model predicts the lowest penetration length.

Toroidal displacement between 2 cm and 4 cm is predicted. In Fig. 16 the penetration length calculated using spherical, lentil and charged ablation models is presented as a function of the corresponding measured penetration length (Table 1 b). The lines show the upper and low limit of the error bars.

The data for the spherical and charged modes are almost the same. The lentil model often predicts lower penetration than those experimentally observed. However, the deviation lies not far from the error bars.

There are four points that obviously deviate from the typical dependence. These points correspond to the conditions with the neutral beam heating of the plasma on TFTR, JET and Heliotron-E. Experimentally determined penetration lengths are 40% less than those calculated.

In Fig. 17 we compare the deviation of the penetration length in the lentil and charged models with the spherical ablation. The difference in the penetration length is inside the 20 % error bars. That means that the available data about the penetration length are not yet satisfactory. More accurate measurements of the temperature profile near the penetration depth are necessary. Also, more accurate information about the pellet size is necessary than the base such as conventional mass measurements and density rise after the pellet injection. It is clear that the effect of the fast ion ablation should be included in the analysis. The effect of fast ions, especially near the pellet poles, is more important than it was thought previously [6]. Checking of this hypothesis should be done on base of the general algorithm described in part 1.

2.2. Local Ablation Rate

One can see the difference in the ablation curves between the spherical (Parks and Charged) and lentil type models. However, the difference is not very large. One may note the increased ablation rate at the last stage of ablation for the lentil case. If we compare the models with the ablation rate (Fig. 16) we can see that experimental ablation is usually higher at the last stage than predictions of any ablation models (even lentil). Sometime it looks as a disk type described in Reference 5. There is now clear understanding of this phenomenon. Perhaps, a faster ablation occurs when the pellet size becomes comparable with the penetration depth for the electrons with $E \sim 6T_e$ that determines the ablation rate. However, we can conclude that the lentil model demonstrates the required tendency.

2.3. Pellet toroidal deflection

Pellet trajectories and toroidal deflection were compared with the experimental data from T-10 tokamak presented in Table 1. For these shots the measured deflection changed from 1 cm up to 5 cm. This dependence is well described by any of the models. Unfortunately, the absolute values of the pellet displacement are almost the same for the models tested. Only the form of the trajectory with higher acceleration at the last stage that is characteristic to the lentil model may be used for distinguishing between the models. This analysis needs much more detailed pellet trajectories than those available now.

2.4. Conclusions

Under conditions without fast particles, database analysis shows that the penetration length may be obtained using any model described. Effect of the hot ions in the NBI heated plasma is substantial and needs additional analysis for penetration prediction even in the hot plasma. Toroidal pellet displacement is also obtained by any of the models considered. The data about the pellet deflection with better spatial resolution are required for comparison of the models with each other.

Table 1 a. Tokamak/Stellarator and Pellet Parameters.

Tokamak, Stellarator	Shot number	B, kGs	I_p, kA	P_{AH}, MW	a, cm	Source	M_i	r_p, cm	$\Delta r_p/r_p$	v_p, cm/s	$\Delta v_p/v_p$
T-10	49945	28.7	382		32	original	1	0.034	0.03	42600	0.003
T-10	49946	28.7	396		32	original	1	0.043	0.03	79700	0.003
T-10	49966	29.7	215		30	original	1	0.055	0.03	58700	0.003
T-10	49968	29.7	203		30	original	1	0.056	0.03	72200	0.003
TFTR	14695		700*	2.5	81.5	[6]	2	0.153	0.03*	140000	0.005
Heliotron-E	25554	19.0	0		30	[32]	2	0.045	0.023*	76000	0.05
Heliotron-E	57443	19*	0	2.5	30	[10]	1	0.065*	0.05*	69000	0.05
Tore-Supra	2687-1	38	944		75	[33]	2	0.13*	0.05*	60000	0.05
Tore-Supra	2687-4	38	944		75	[33]	2	0.13*	0.05*	60000	0.05
Tore-Supra	4150		1410		75	[33]	2	0.13*	0.05*	60000	0.05
Tore-Supra	4153	39.2	1410		75	[33]	2	0.13*	0.05*	60000	0.05
Alcator-C	0.3nov83.060				16.5	[34]	2	0.075	0.05	60000	0.05
JET	20732				113	[8]	2	0.135	0.05	50500	0.003
JET	19398		3000	9.0	113	[9]	2	0.135	0.05	140000*	0.003
JET	26670			9.0	113	[9]	2	0.2	0.05	115300	0.003
TFTR	27560				81.5	[9]	2	0.15	0.05	125000	0.005
ISX-B	summary				27	[7]	1	0.057	0.05	90000	0.005

Table 1 b. Plasma Parameters.

Tokamak, Stellarator	Shot number	$n_e(r)$, 10^{13}cm^{-3}	$\Delta n_e/n_e$	$T_e(r)$, eV	$\Delta T_e/T_e$	L, cm	ΔL, cm
T-10	49945	$7.73[1-(r/a+5)^2]$	0.1	$1055[1-(r/a+0.5)^2]$	0.05	13	1.32
T-10	49946	$7.55[1-(r/a+0.3)^2]$	0.1	$1129[1-(r/a+0.5)^2]$	0.05	20	2.03
T-10	49966	$4.29[1-(r/a+4)^2]^{1.5}$	0.1	$1369[1-(r/a+0.5)^2]^{2.5}$	0.05	20	2.03
T-10	49968	$4.73[1-(r/a+3)^2]^{1.5}$	0.1	$768[1-(r/a+0.5)^2]^{1.5}$	0.05	36	3.61
TFTR	14695	$1.62[1-(r/a)^2]^2+0.18$	0.1*	$3150[1-(r/a)]+50$	0.1*	49	8.90
Heliotron-E	25554	$2.0[1-(r/a)^5]$	0.1	$1052[1-(r/a)^{1.5}]$	0.1	25	4.47
Heliotron-E	57443	$5.0[1-(r/a+10)^4]^6$	0.1	$500[1-(r/a+10)^4]^7$	0.1	28	5.40
Tore-Supra	2687-1	$2.0[1-(r/a)^2]$	0.1	$2900[1-(r/a)]$	0.1	46	8.90
Tore-Supra	2687-4	$3.85[1-(r/a)^2]$	0.1	$2000[1-(r/a)]$	0.1	57	11.0
Tore-Supra	4150	$1.25[1-(r/a)^2]$	0.1	$3800[1-(r/a)]$	0.1	37*	7.16
Tore-Supra	4153	$2.9[1-(r/a)^2]$	0.1	$3000[1-(r/a)]$	0.1	42*	8.10
Alcator-C	0.3nov83.060	$55[1-(r/a)^2]^{0.6}$	0.1	$1.48\exp(-2.52r^2/a^2)$	0.1	12*	2.30
JET	20732	$2.3[1-(r/a)^4]$	0.1	$2360[1-(r/a)^2]$	0.1	49	9.20
JET	19398	$2.4[1-(r/a)^{1.5}]$	0.1	$4490[1-(r/a)]$	0.1	44	8.20
JET	26670	$5.0[1-(r/a)^4]^{0.3}$	0.1	$3100[1-(r/a)]$	0.1	61	11.4
TFTR	27560	$2.5[1-(r/a)^2]$	0.1	$3200[1-(r/a)]$	0.1	58	10.8
ISX-B	summary	$2.[1-(r/a)^2]$	0.1	$1400[1-(r/a)^2]^2$	0.1	25	4.67

Part 3. Deuterium pellet ablation in the LHD

Pellet penetration into the LHD plasma has been analyzed in detail in the document "Development of High Speed Pellet Injector" [35]. The analysis has been performed on base of the Milora and Foster model [2] and a code for penetration simulations developed at ORNL.

In this part we compare the results of the NIFS simulations with the models discussed in part 1, 2. Program EVAPMODL developed at STU (St. Petersburg) has been used for the simulation of the multipellet fueling.

We have simulated pellet penetration into the LHD in the following layout of the experiments:

Table 2. Specifications of the LHD.

- Main parameters of the LHD.

major radius, m	3.9
minor axis (vertical), m	0.6
major axis (horizontal), m	0.9
plasma volume, m^{-3}	41.53

- Main plasma parameters.

line averaged density, cm^{-3}	4×10^{19}
density profile, cm^{-3}	$6\times10^{19}(1-(r/a)^2)$
temperature profile, eV	$4\times10^{3}(1-(r/a)^2)^2$
volume averaged density, cm^{-3}	3×10^{19}
Total amount of the particles in the target plasma	1.3×10^{21}

Calculations of the penetration length have been performed for the injection in horizontal plain along the major axis.

3.1. Ablation Scaling for the High Plasma Parameters Region

As the plasma parameters and pellet parameters in the LHD-experiments will be much higher than those considered in part 1 it is useful to check the ablation scaling for the temperature region T_e up to 5

keV, electron density n_e up to 2×10^{14} cm^{-3} and the pellet radius up to 0.5 cm centimeter and various pellet materials (M_i= 1,2,3).

The ratio of the ablation rate density near the axis of deuterium pellet to the value predicted by Parks scaling is shown in Table 3. (The pellet radius was equal to 0.05 cm for this simulation).

Table 3 Calculated ablation rate density normalized by the value predicted by Parks scaling.

T_e, eV	500	5000
n_e, 10^{13} cm^{-3}		
1	2.906	3.31
16	4.01	4.88

A significant increase of the ablation is seen with growth of the plasma parameters. The similar increase was observed when the pellet radius was changed from 0.05 cm up to 0.5 cm. At $n_e=16\times10^{13}cm^{-3}$ and T_e=5000 eV the corresponding dependence is presented in Table 4.

Table 4 Dependence of ablation rate on pellet radius.

$r_{p,cm}$	*0.05*	*0.15*	*0.5*
ratio	*4.88*	*5.59*	*6.33*

With growth of the pellet material mass M_i we have observed a growth of the ablation ratio as well. The results are presented in Table 5.

Table 5 Dependence of ablation rate on pellet material mass.

M_i	1	2	3
ratio	6.07	6.33	6.41

These deviations of the ablation rate from the Parks scaling may be taken into account by multiplication of the Parks' formula on the function:

$$f_1=\left(\frac{n_e}{10^{13}}\right)^{0.12}\left(\frac{T_e}{500}\right)^{0.08}\left(\frac{r_p}{0.05}\right)^{0.11}M_i^{0.05}\frac{2.65}{2} \qquad (71)$$

Finally, a new scaling for the ablation has the form

$$dN/dt = 3.46\times10^{14} n_e^{0.453} T_e^{1.72} r_p^{1.443} M_i^{-0.283} \tag{72}$$

This scaling predicts larger ablation rates than the Parks' formula. At the plasma parameters typical for the contemporary experiments the deviation is not very large (30 %). However, at the maximum LHD-parameters or ITER-parameters the ablation rate according to this scaling will be 3 times higher than what Eq. (1) predicts. The dependence on the density and radius is changed most significantly.

3.2. Modifications of the Charged Mode for a Deuterium Pellet

Charged mode described in part 1 for the hydrogen case should be modified in the case of deuterium as follows.

Energy loss function for deuterium is less than that for the hydrogen

$$L_d = 1.93\times10^{-16} E^{0.4} \times 2^{-0.4} \tag{73}$$

Due to larger mass of atoms the pellet is charged up to a higher potential

$$e\Delta\phi = 1.7\left(T_e/e\right) + \left(1/2\right)\ln M_i \left(T_e/e\right) = 2.05\left(T_e/e\right) \tag{74}$$

These two factors decrease the ablation rate by a factor of 0.73 in comparison with the lentil ablation of the deuterium pellet

$$dN/dt = 3.46\times10^{14} n_e^{0.453} T_e^{1.72} r_p^{1.443} M_i^{-0.283} \times 0.73 \tag{75}$$

Expression for the toroidal acceleration also should be changed as follows

$$dv_z/dt = \left(2/3\right)\left(3/4\pi\right) U n_a^{-1} (0.453)(3.465\times10^{14}) \\ n_e^{-0.547} T_e^{1.72} r_p^{-1.557} M_i^{-0.283} D n_e \exp\left(-2.05/3\right) \tag{76}$$

3.3. Simulation of the Pellet Penetration into LHD

Ablation rates for the deuterium pellet with velocity v_p =1 km/s and r_p=0.15 cm calculated using Parks' scaling , charged pellet and lentil models are presented in Fig. 18. Plasma density profile $n_e(r)$ and electron temperature profile $T_e(r)$ are assumed to be as follows:

$$T_e(r) = 4000\left[1-\left(r/a\right)^2\right]^2, \qquad n_e(r) = 6\times 10^{13}\left[1-\left(r/a\right)^2\right], \qquad \text{a= 90 cm.} \quad (77)$$

The pellet penetration radius is equal to 38.5 cm, 43 cm and 50 cm for the Parks' formula, charged ablation and lentil ablation correspondingly. Dependencies of the penetration length on the pellet velocity are shown in Fig. 19. The previous simulation of the pellet penetration [34] is presented as well.

Penetration length is proportional to the pellet velocity in the power equal to 0.33, 0.32, 0.27 for the Parks' scaling, charged pellet mode and lentil mode. The result from the Parks' scaling is in agreement with the penetration analyzed for the linear profiles of the plasma parameters[8]. Disagreement of our simulation with the other simulation by the ORNL code may be related to a version of the ORNL program that uses the sound velocity scaling [1] for the ablation rate that gives the higher ablation rates than formula (1) in the low temperature region [5]. At the plasma center the self limiting effect that was taken into account by the ORNL-program significantly changes the penetration.

Simulation of the LHD and T-10 fueling using two pellets instead of one with the same total mass has shown that the penetration depth for this option is less than in the case of one large pellet. The corresponding results are presented in Fig. 20 (a, b). So, we conclude that single pellet injection is preferable way of fueling.

3.4. Conclusions

The deuterium pellet penetration into the Large Helical Device has been studied.

Two-dimensional ablation model has been developed using a kinetic approach to the heat flux penetration through the cloud and hydrodynamic scaling for the gas expansion [6]. Heat fluxes by both thermal and hot electrons and ions have been taken into account. Thermal ion heat flux is significant near the pellet poles where the electron ablation is negligible. Effects of the electrostatic and plasma shielding have been considered.

It is shown that the ablation rate exceeds the Parks scaling only by a factor of 1.3 for the kinetic model with the moderate plasma parameters. However, two-dimensional ablation by electrons leads to change of the pellet shape from sphere to lentil as observed in case of the impurity pellet. This

modification of the pellet form requires new algorithm of the ablation rate calculations. Pellet charging due to electron flux changes significantly the distribution of the ablating heat fluxes. However, the total ablation rate in the case of charged pellet is almost the same as for the non charged pellet. This is caused by increase of the ion heat flux. There, the ion ablation becomes comparable with the electron one.

It is possible to neglect the plasma shielding because the instabilities in the plasma cloud reduce the time of the plasma shift from the electron heat path. Plasma optical length is less than the neutral one.

Pellet acceleration in a plasma with current has been investigated and expressions for the acceleration have been obtained for the spherical, lentil and charged pellet ablation models.

The highest acceleration is expected for the lentil case and the lowest one for the charged pellet. The calculated values of the toroidal deflection and acceleration correlate with the experimental data obtained on T-10.

Experimental database on the ablation has been formed and analyzed. Accuracy analysis has shown that the electron temperature and pellet radius measurements are most important for the penetration analysis. Typical experimental errors in the penetration depth is about ~15%, which is not sufficient for distinguished test of the ablation models.

Influence of the hot ion ablation has been observed in the Heliotron-E, TFTR, JET.

Finally, a new ablation scaling for the plasma parameters close to the reactor has been proposed. It predicts higher ablation rate than the Parks' scaling. Deviation up to 2.8 times is expected at T_e=5000 eV , n_e=16×10^{13} and r_p=0.5 cm. Penetration scaling is close to the $L \sim v_p^{0.33}$. Penetration in LHD is expected up to 0.3-0.4 of the minor radius for the maximum pellet velocity of ~3 km/s. This result confirms the possibility of the fueling of the central zone of the LHD using the pellet injector designed at NIFS [34].

Acknowledgment

Author is grateful to Prof. S. Sudo for initiation and support of this work and numerous fruitful discussions. I also would like to thank my colleagues at STU who supported this work: S.N. Ushakov, V.Yu. Sergeev, K. Khlopenkov, I. Miroshnikov, D. Poliakov, and M. Svoiskaya.

The work was performed under the contract with NIFS.

References

1. Parks, P.B., Turnbull, R.J., Foster, C.A., Nucl. Fusion **17** (1977) 539.
2. Milora, S.L., Foster, C.A., IEEE Trans. Plasma Sci. **PS-6** (1978) 578.
3. Parks, P.B., Turnbull, R.J., Phys. Fluids **21** (1978) 1735.
4. Kuteev, B.V., Sergeev, V.Yu., Tsendin, L.D., Sov. J. Plasma Phys. **10** (1984) 675
5. Kuteev, B.V., Umov, A.P., Tsendin L.D., Sov. J. Plasma Phys. **11** (1985) 236.
6. Houlberg, W.A., Milora S.L., Attenberger, S.E., Nucl. Fusion **28** 1988 595.
7. Gouge, M.J., Houlberg, W.A., Milora S.L., Fusion Technol. **19** (1991) 95.
8. Houlberg, W.A., Attenberger, S.E., Baylor, L.R., et al. Nuclear Fusion **32** (1992) 1951.
9. Baylor, L.R., Schmidt G.L., Houlberg, W.A., et al. Nucl. Fusion **32** (1992) 2177.
10. Nakamura, Y., Kiji, S., Wakatani, M., et al. Nuclear Fusion **32** (1992) 2229.
11. Egorov, S.M., Kuteev B.V., Miroshnikov I.V., et al. Nucl. Fusion **32** (1992) 2035.
12. Rozhansky, V.A., Sov. J. Plasma Physics **15** (1989) 638.
13. Kaufmann, M., Lackner, K., Lengyel, L.L., et al., Nucl. Fusion **26** (1986) 171.
14. Veselova, I.Yu., Rozhansky, V.A., Sov. J. Plasma Physics **17** (1991) 817.
15. Parks, P.B., Nucl. Fusion **32** (1992) 2137.
16. Parks, P.B., Nucl. Fusion **20** (1980) 311.
17. Lengyel, L.L., Nucl. Fusion **29** (1989) 37.
18. Parks, P.B., Nucl. Fusion **31** (1991) 1431.
19. Milora, S.L., New Algorithm for Computing the ablation of Hydrogenic Pellet in Hot Plasmas. Rep. ORNL-TM-8616, Oak Ridge National Lab. (1983)
20. Nakamura, Y., Nishihara, H., Wakatani, M., Nucl. Fusion **26** (1986) 907.
21. Dubois, M.A., Sabot, R., Pegourie, B., et al., Nucl. Fusion **32** (1992) 1935.
22. Post, D.E., Mikkelsen D.R., Hulse, R.A., et al., J. Fusion Energy **1** (1981) 129.
23. Kalashnikov, N.P., Remizovich, V.S., Ryazanov M.I., Collisions of Fast Charged Particles in Solids (in Russian). Atomizdat, Moscow (1980).
24. Egorov, S.M., et al. in Proc. 13-th Int. Conf.on Plasma Phys. and Control. Nucl. Fus. Res. 1990, Washington, **v. 1**, p. 599.
25. Durst, R.D., Rowan, W.L., Austin, M.E., et al. Nucl.Fusion **30** (1990) 3.
26. Spitzer, Jr., L., Grove, D.J., Johnson, W.E., Tonks, L., Westendorp, W.R., Problems of the Stellarator as a Useful Power Source, USAEC Report NYO 6047 (1954).
27. Laframboise, J. G.,UTIAS Report, June 1966, No. 100.
28. Chen, F.F., in Plasma Diagnostic Techniques. ed. Huddlstone R.H. and Leonard S.L., Academic Press, NY, (1965) 113.
29. Gill, R.D., Edwards, A.W.,Weller, A., Nucl. Fusion **29** (1989) 821.

30. TFR Group, Europhys.Lett., **2** (1986) 267.
31. Braginski, S.I., in Reviews of Plasma Physics, Vol. 1, Consultants Bureau, New York (1965)205.
32. Sudo, S., Zushi, H., Kondo, K., et al. Nucl. Fusion **31** (1991) 2349.
33. Drawin, H.-W., Dubouis, M.A., Nucl. Fusion **32** (1992) 1615.
34. Dunning, M.J., Mayer, F.J., Kammash, T., Nucl. Fusion **30** (1990) 919.
35. Sudo, S. IAEA-meeting on Pellet Injection, Naka, Japan, May 1993.

Figures Captions

Fig. 1. Schematic illustration of the pellet ablation process. The picture is obtained on T-10 tokamak using a high speed camera with exposure time 5×10^{-6} s. Plasma parameters: $n_e=2\times10^{13}$ cm^{-3}, $T_e=500$ eV, $r_p=0.067$ cm, $v_p=6\times10^4$ cm/s. Electrons move to the pellet surface along the magnetic field lines. They penetrate through the double layer at the boundary of hot and cold plasma or the sheath near the ionization radius. They are decelerated in the cold fully ionized and partially ionized plasma as well as in the neutral cloud. The density of the neutral cloud decreases to the pellet poles. The heat flux of the thermal and hot ion is isotropic because the ion gyro radii are comparable to or more than the pellet radius.

Fig. 2. The electron and ion heat flux versus the optical length of the screening cloud. Thermal fluxes have a Maxwellian distribution with the temperature $T_e=T_i=500$ eV. The hot ions have a classical distribution function with one energy source at 25 keV and volume averaged power 0.5 W/cm^3. Density of the erosion energy flux as a function of the cloud optical length Sn is shown as well. Pellet radius r_{po} is equal to 0.05 cm.

1- density of the electron heat flux without the angular part of $f(v)$;

2- correct heat flux density for the thermal electron ;

3- density of the hot ion heat flux without the angular part of $f(v)$;

4- correct heat flux density for the hot ions;

5- heat flux density for the thermal ions without the angular part of $f(v)$;

6- correct heat flux density for the thermal ions;

7- density of the erosion energy flux induced by electron heat flux Q_{eo};

8- the same for the thermal ion heat flux Q_{io};

9- the same for the hot ion heat flux Q_{ho}.

Fig. 3. Schematic diagram of the ablation for the α not equal to 0.
The longitudinal electron heat flux Q_{eo} in our assumptions is changed to the radial heat flux with lower density. The longitudinal optical length of the cloud does not change if the density in the cloud and radial optical length are decreased simultaneously. A difference in the volumes heated by the original heat flux and the assumed exists. However, it is not very significant in case when the main optical length is formed near the pellet surface.

Fig. 4. Ablation rate calculated using the algorithm proposed (curve 1) and a standard one (curve 2). Pellet and plasma parameters are presented in Eq. (25).

Fig. 5. Heat fluxes onto the surface of charged pellet. Potential drop in the sheath is assumed to be equal to $e\phi=1.7\,T_e$.

a)- $\alpha=0$; b)- $\alpha=\pi/4$; c)- $\alpha=\pi/2$.

1- Q_S, 2- Q_e, 3- erosion heat flux, 4- electron part of the erosion heat flux.

Pellet and plasma parameters are presented in Eq. (25).

Fig. 6. Poloidal distribution of the heat fluxes for the charged pellet case.

a)- ablating heat flux density at the cloud boundary;

b)- poloidal distribution of the ablating rate density;

1-electron ablation without charging of the pellet;

2- summary ablation of the charged pellet.

Pellet and plasma parameters are presented in Eq. (25).

Fig. 7. Electron distribution function for the counter current side of the pellet.

1- non shifted Maxwellian distribution, 2- shifted Maxwellian distribution $(u/v_{Te}=0.1)$, 3- distribution used for the acceleration determination $(n_e=n_{eO}+Dn_e)$.

Fig. 8. Parameters of the hydrogen pellet trajectory. ($r_p=0.075$ cm, $v_p=6.6\times10^4$ cm/s, $n_e=3\times10^{13}[1-(r/a)^2]$, $T_e=1200[1-(r/a)^2]^2$).

1-spherical ablation; 2- lentil ablation; 3- charged ablation.

Fig. 9. Ablation rate and trajectory parameters for the charged pellet ablation.

Fig. 10. Characteristics of the high energy electrons' interaction with hydrogen pellet.

a)- pellet optical length; b)- critical penetration energy; c)- relative energy losses.

Fig. 11. Electron energy losses during penetration through the pellet .

a)-1-E_O=100 keV, 2-200, 3-300, 4-400, 5-500;

b)- 1-E_O=200 keV, 2-400, 3-600, 4-800, 5-1000.

Fig. 12. Electron energy E after penetration through the pellet versus the poloidal angle α.

a)- r_p=0.075 cm; b)- r_p=0.15 cm.

1-E_O=100 keV, 2-200, 3-300, 4-400, 5-500.

Fig. 13. Parameters of interaction of the high energy electrons with a pellet.

(n_b=10^8 cm^{-3}).

a)- the total power onto the pellet surface;

b)- the ablating power;

c)- the part of energy spent on the ablation.

Fig. 14. Heat balance on the pellet surface in a plasma with hot electrons.
a)- $Q_{he}=Q_e$; b)- $Q_{he}=2Q_e$.
1- thermal heat flux; 2- hot electrons' flux; 3- summary flux; 4-erosion energy flux.

Fig. 15. Deuterium pellet ablation and toroidal deflection in Tore-Supra.
a)- ablation rate; b)- toroidal displacement.
1-Parks scaling; 2-charged mode; 3- lentil mode.

Fig. 16. Calculated penetration length versus experimental penetration length.
a)- Parks scaling; b)- charged mode; c) lentil mode.
Lines show the upper and lower boundary of the errors.

Fig. 17. Calculated penetration length versus Parks' scaling.
Lines correspond to 0.8 and 1 of the penetration length calculated using the Parks' scaling in conditions of Table 1.

Fig. 18. Deuterium pellet penetration into the LHD. (r_p=0.15 cm, v_p=1 km/s.)
1- Parks' scaling; 2- charged mode; 3- lentil mode.

Fig. 19. Dependencies of the penetration length on the pellet velocity for the LHD.

Fig. 20. Single and double pellet fueling with the same amount of the particles in the pellet. a)- T-10; b)- LHD.

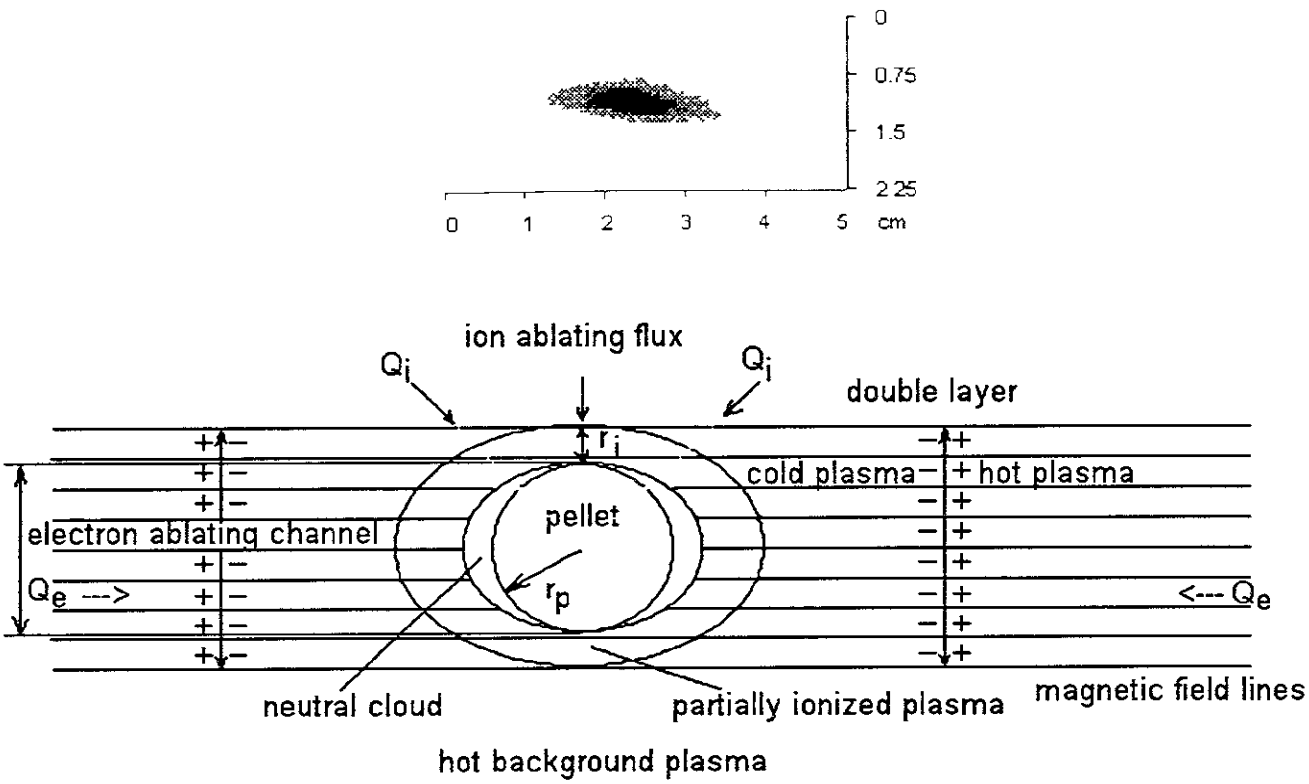
0
0.75
1.5
2.25
0
1
2
3
4
5
cm
ion ablating flux
Q_i
Q_i
double layer
r_i
cold plasma
hot plasma
pellet
electron ablating channel
Q_e --->
r_p
<--- Q_e
neutral cloud
partially ionized plasma
magnetic field lines
hot background plasma

Fig.1

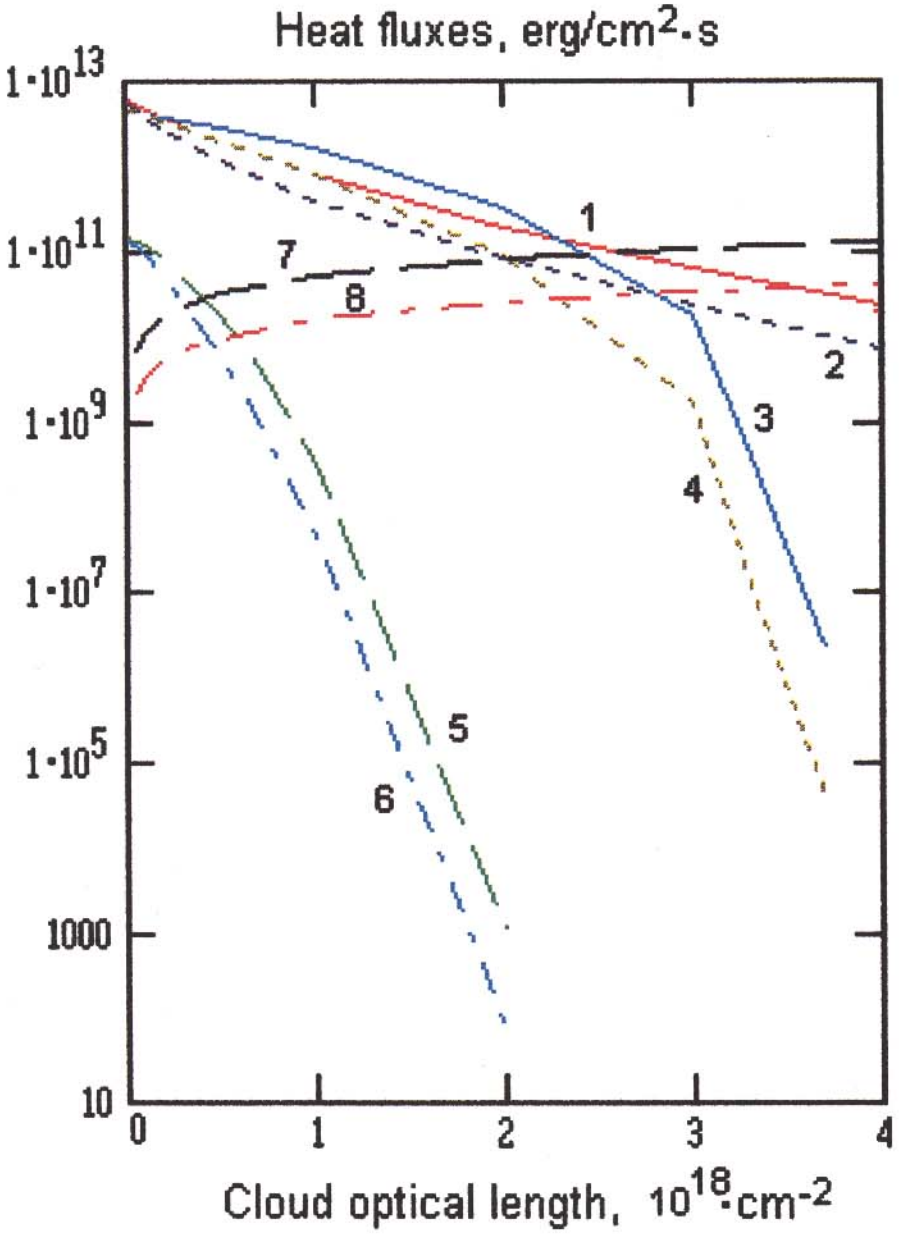
Heat fluxes, erg/cm2·s
1·10^13
1·10^11
1·10^9
1·10^7
1·10^5
1000
10
0
1
2
3
4
Cloud optical length, 10^18·cm^-2
1
2
3
4
5
6
7
8

Fig. 2 a

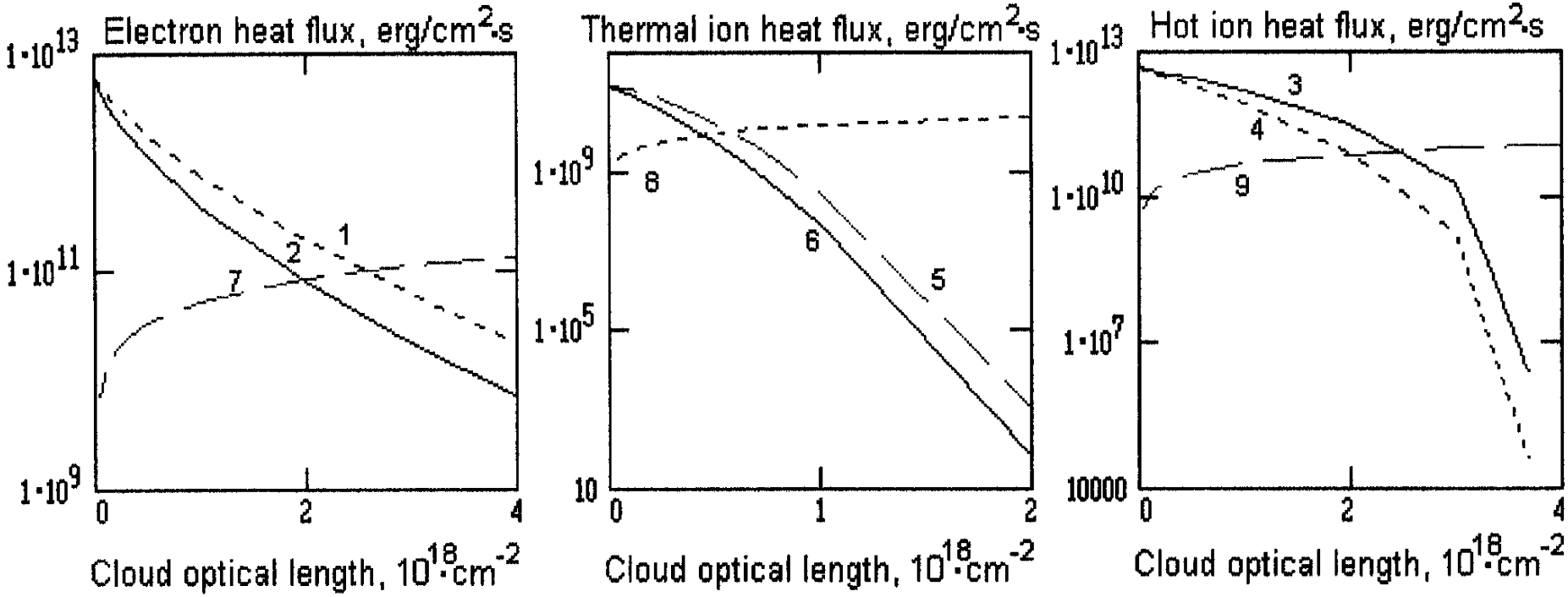
Electron heat flux, erg/cm²·s
1·10¹³
1·10¹¹
1·10⁹
0
2
4
1
2
7
Cloud optical length, 10¹⁸·cm⁻²
b
Thermal ion heat flux, erg/cm²·s
1·10⁹
1·10⁵
10
0
1
2
8
6
5
Cloud optical length, 10¹⁸·cm⁻²
c
Hot ion heat flux, erg/cm²·s
1·10¹³
1·10¹⁰
1·10⁷
10000
0
2
4
3
4
9
Cloud optical length, 10¹⁸·cm⁻²
d

Fig. 2

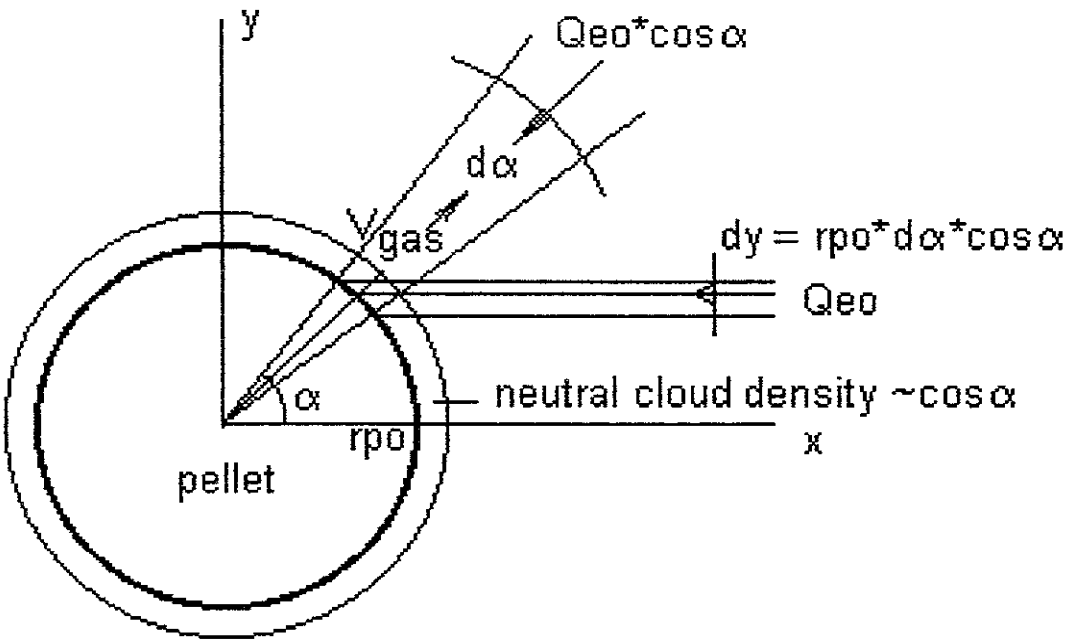
y
Qeo*cosα
dα
V gas
dy = rpo*dα*cosα
Qeo
α
neutral cloud density ~cosα
rpo
x
pellet

Fig. 3

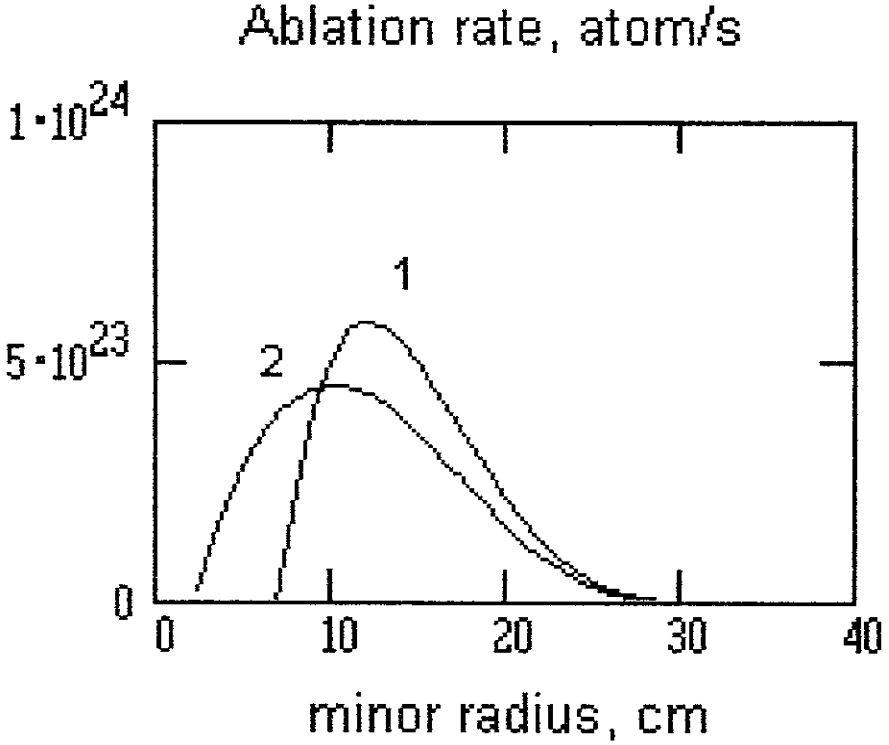
Ablation rate, atom/s
1·10^24
5·10^23
0
1
2
0
10
20
30
40
minor radius, cm

Fig.4

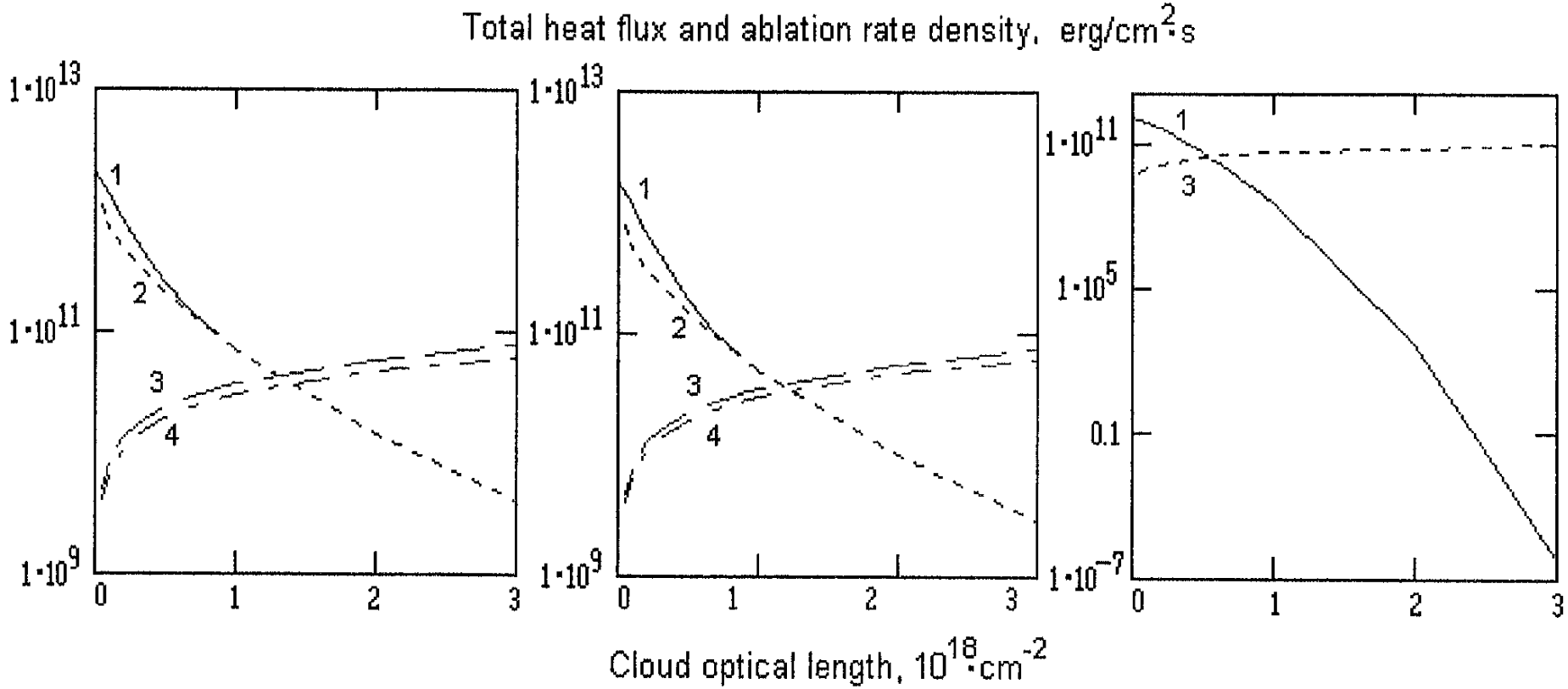
Total heat flux and ablation rate density, erg/cm^2·s
$1\cdot10^{13}$
$1\cdot10^{11}$
$1\cdot10^{9}$
$1\cdot10^{13}$
$1\cdot10^{11}$
$1\cdot10^{9}$
$1\cdot10^{11}$
$1\cdot10^{5}$
0.1
$1\cdot10^{-7}$
1
2
3
4
0
1
2
3
Cloud optical length, 10^{18}·cm^{-2}
a
b
c

Fig. 5

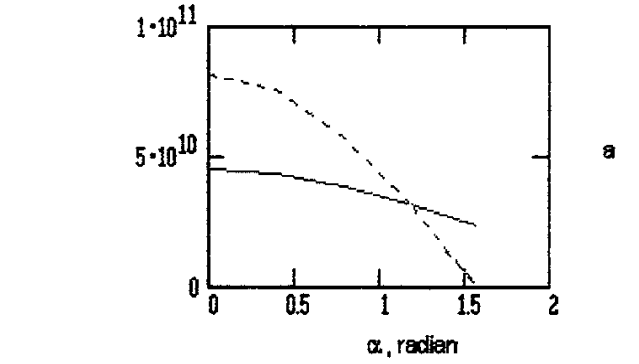

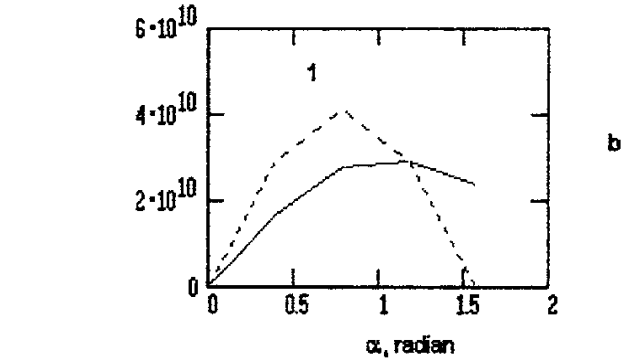

Fig. 6

electron distribution function

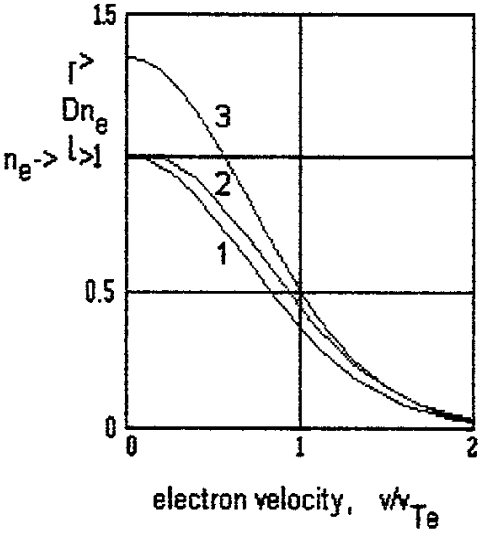

Fig. 7

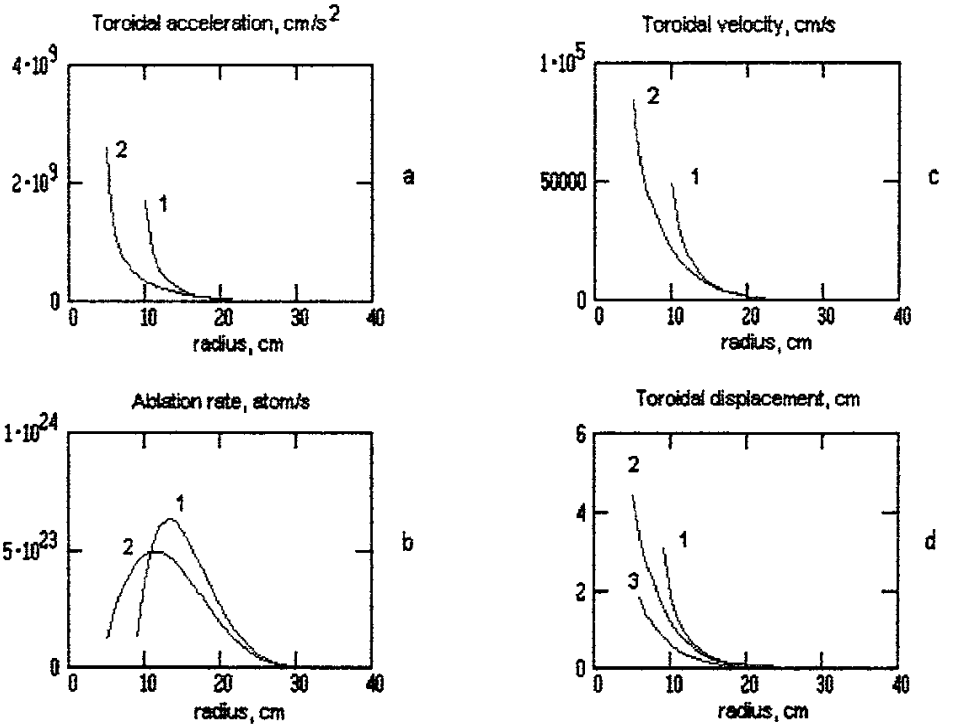
Toroidal acceleration, cm/s 2
4·10 9
2·10 9
0
2
1
a
0 10 20 30 40
radius, cm
Toroidal velocity, cm/s
1·10 5
50000
0
2
1
c
0 10 20 30 40
radius, cm
Ablation rate, atom/s
1·10 24
5·10 23
0
1
2
b
0 10 20 30 40
radius, cm
Toroidal displacement, cm
6
4
2
0
2
1
3
d
0 10 20 30 40
radius, cm

Fig. 8

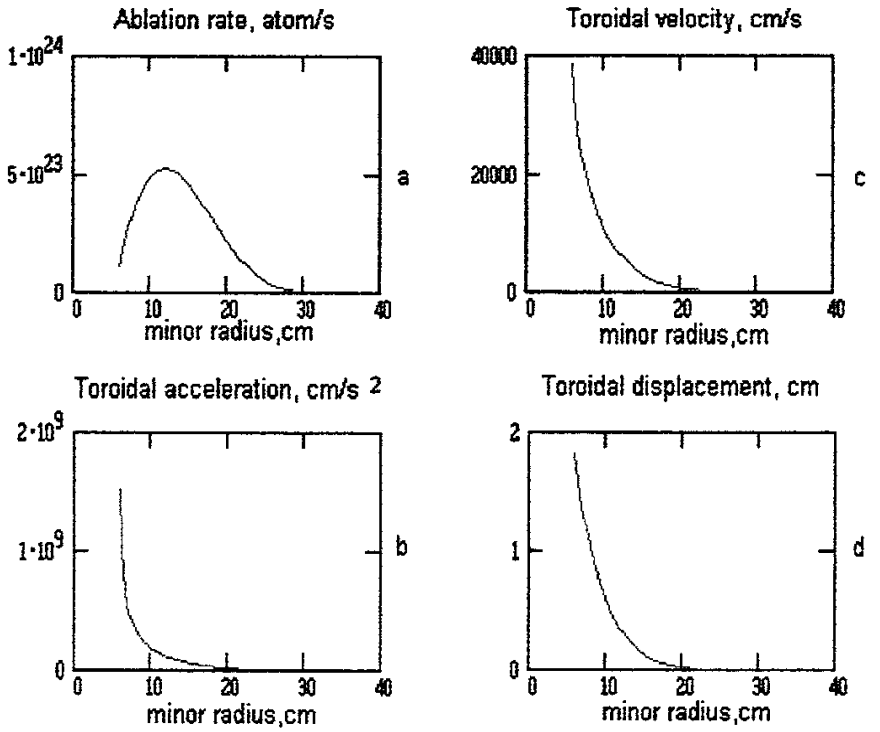
Ablation rate, atom/s
1·10 24
5·10 23
0
a
0 10 20 30 40
minor radius,cm
Toroidal velocity, cm/s
40000
20000
0
c
0 10 20 30 40
minor radius,cm
Toroidal acceleration, cm/s 2
2·10 9
1·10 9
0
b
0 10 20 30 40
minor radius,cm
Toroidal displacement, cm
2
1
0
d
0 10 20 30 40
minor radius,cm

Fig. 9

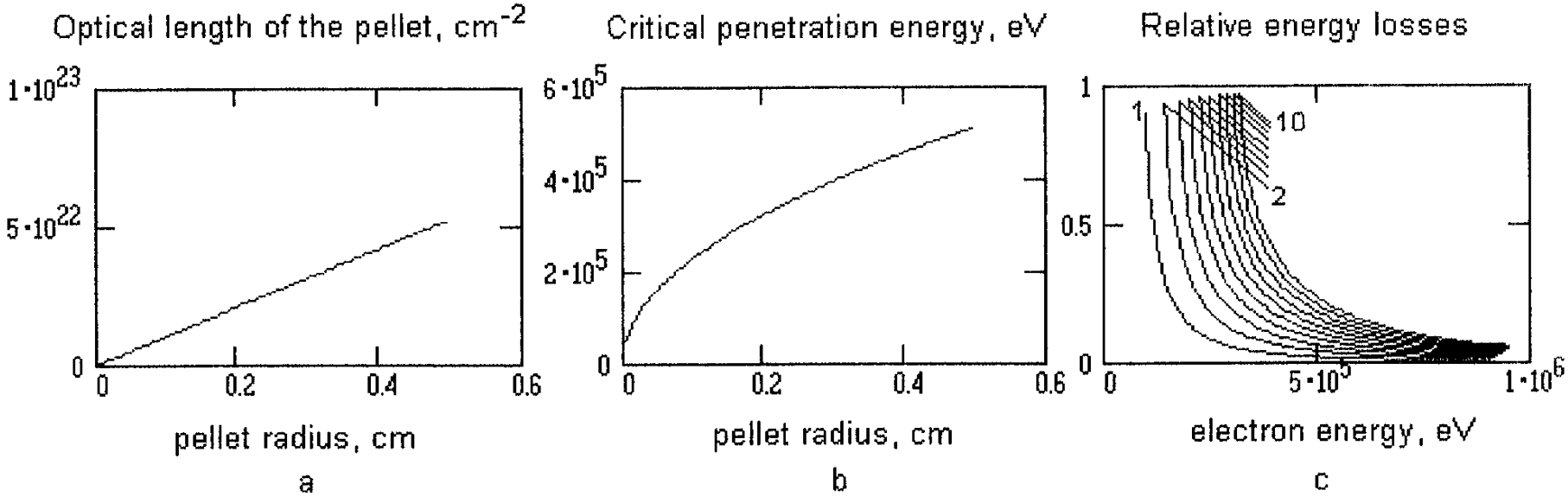
Optical length of the pellet, cm-2
1·10^23
5·10^22
0
0
0.2
0.4
0.6
pellet radius, cm
a
Critical penetration energy, eV
6·10^5
4·10^5
2·10^5
0
0
0.2
0.4
0.6
pellet radius, cm
b
Relative energy losses
1
0.5
0
1
10
2
0
5·10^5
1·10^6
electron energy, eV
c

Fig. 10

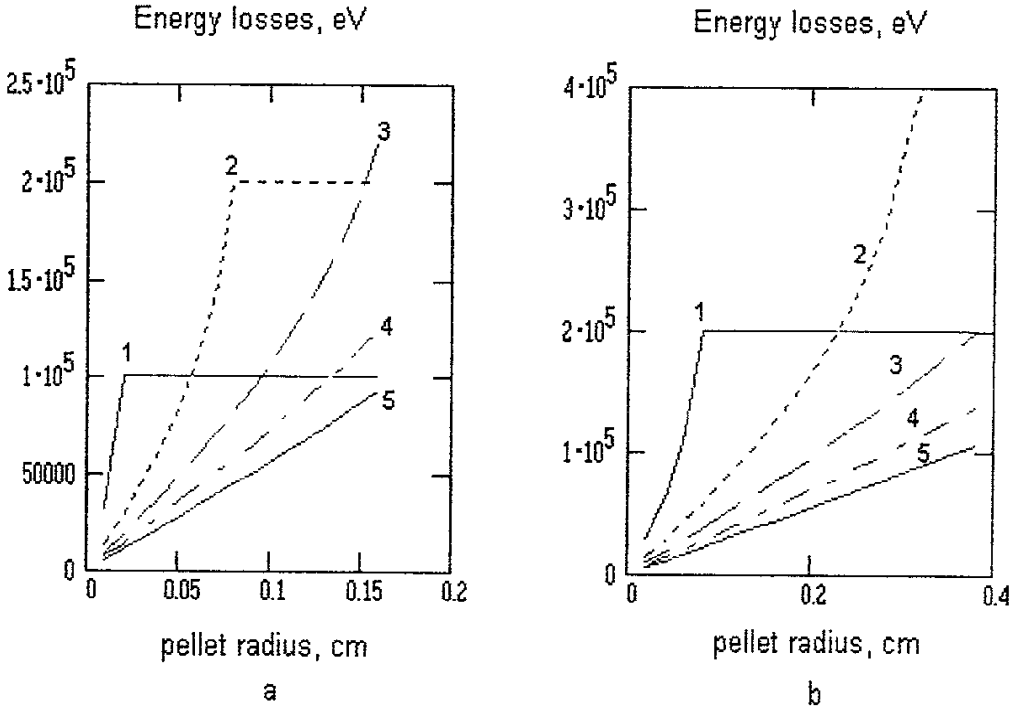
Energy losses, eV
2.5·10^5
2·10^5
1.5·10^5
1·10^5
50000
0
0
0.05
0.1
0.15
0.2
1
2
3
4
5
pellet radius, cm
a
Energy losses, eV
4·10^5
3·10^5
2·10^5
1·10^5
0
0
0.2
0.4
1
2
3
4
5
pellet radius, cm
b

Fig. 11

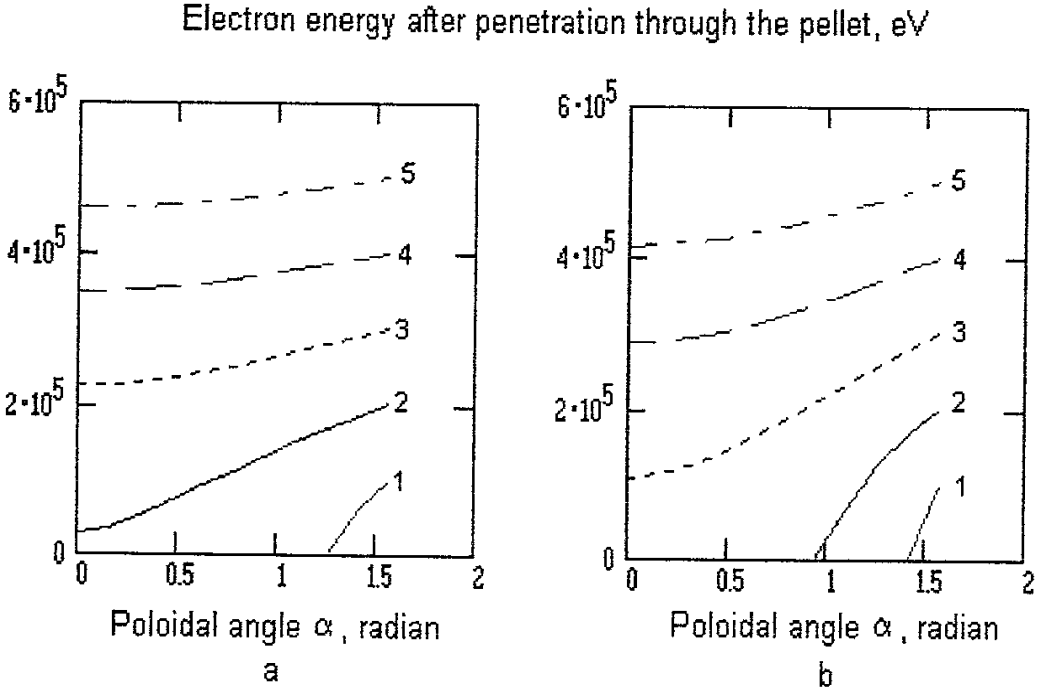
Electron energy after penetration through the pellet, eV
6·10^5
4·10^5
2·10^5
0
0
0.5
1
1.5
2
1
2
3
4
5
Poloidal angle α, radian
a
6·10^5
4·10^5
2·10^5
0
0
0.5
1
1.5
2
1
2
3
4
5
Poloidal angle α, radian
b

Fig. 12

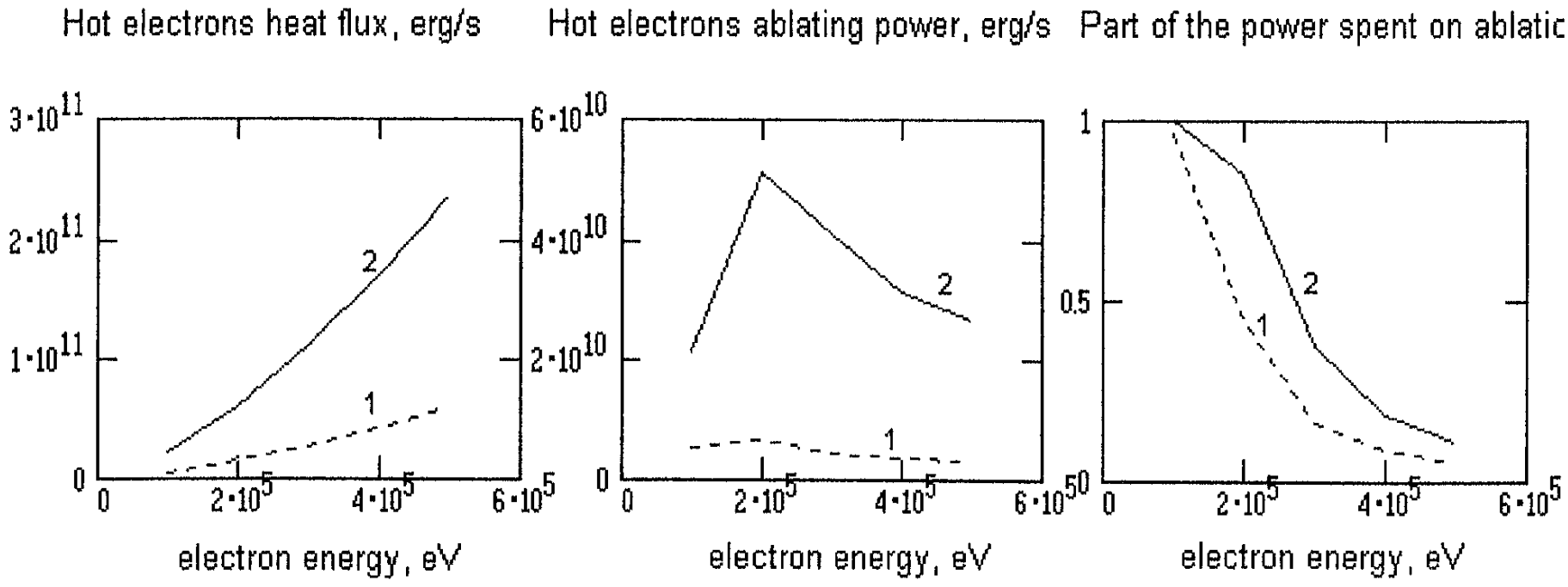
Hot electrons heat flux, erg/s
Hot electrons ablating power, erg/s
Part of the power spent on ablatic
3·10^11
2·10^11
1·10^11
0
6·10^10
4·10^10
2·10^10
0
1
0.5
0
2·10^5
4·10^5
6·10^5
50
1
2
electron energy, eV
a
b
c

Fig. 13

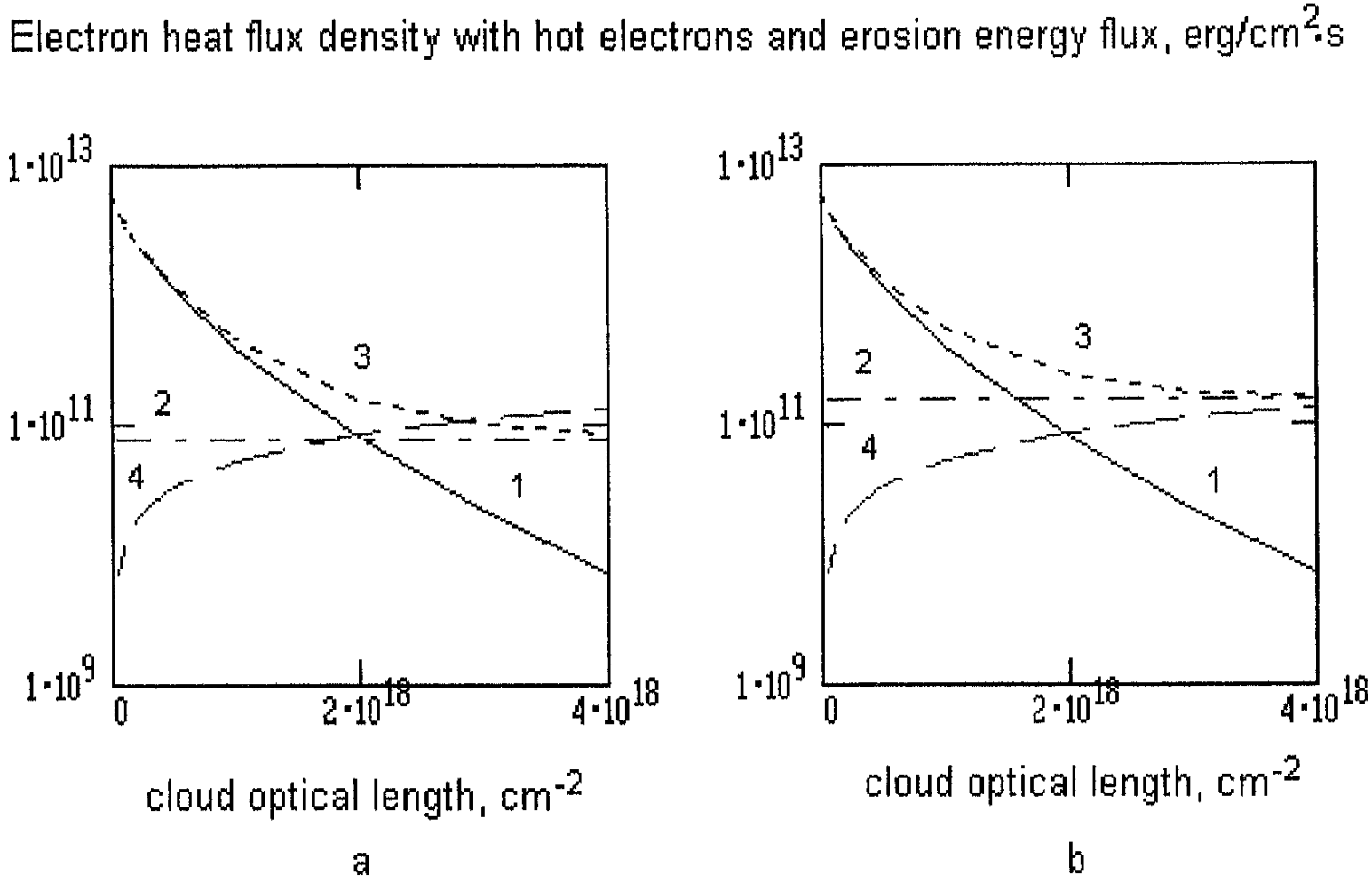
Electron heat flux density with hot electrons and erosion energy flux, erg/cm2·s
1·10^13
1·10^11
1·10^9
0
2·10^18
4·10^18
1
2
3
4
cloud optical length, cm^-2
a
1·10^13
1·10^11
1·10^9
0
2·10^18
4·10^18
1
2
3
4
cloud optical length, cm^-2
b

Fig. 14

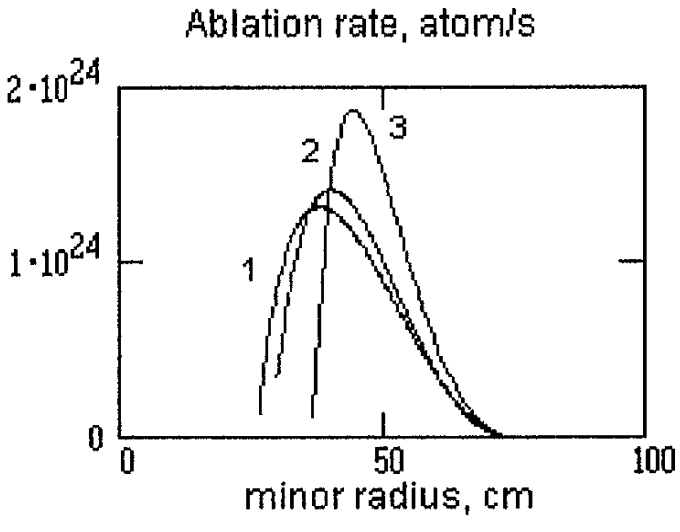

Fig.15 a

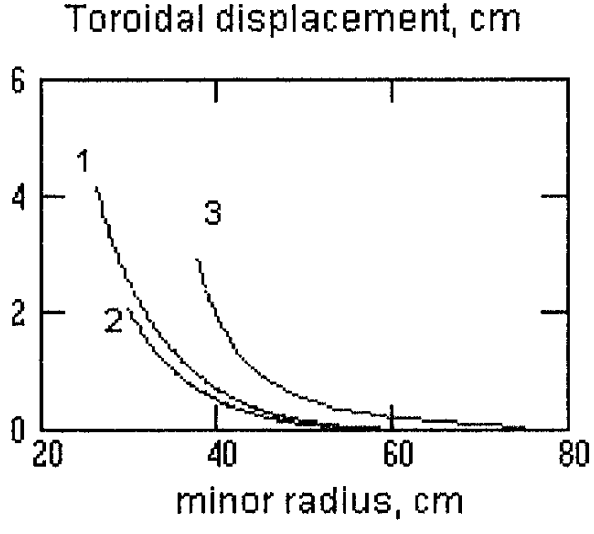

Fig.15 b

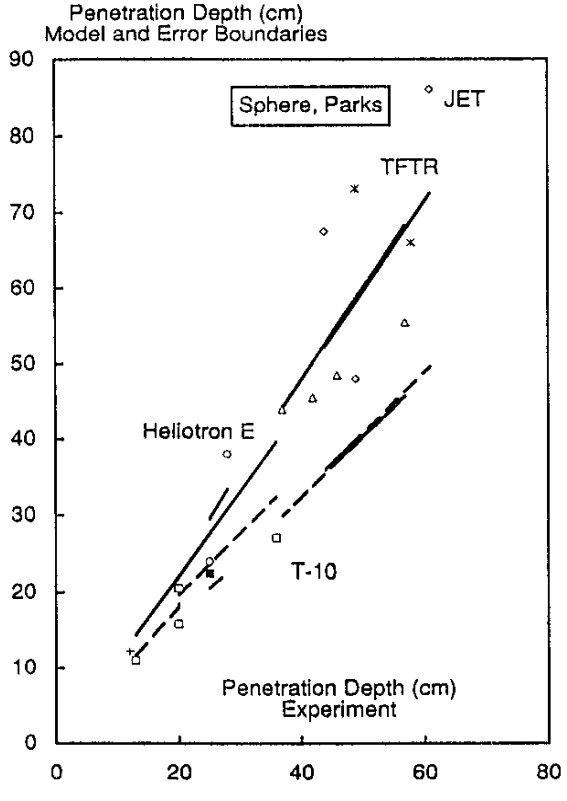

Fig.16 a

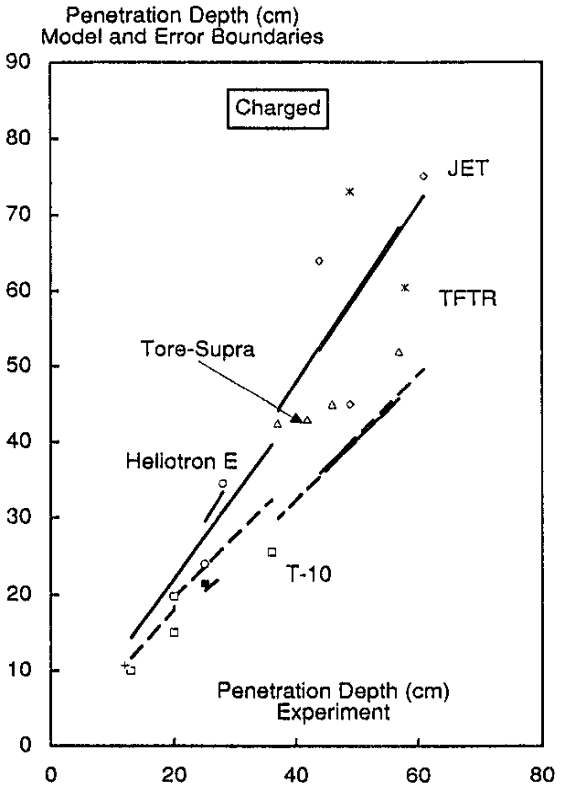

Fig.16 b

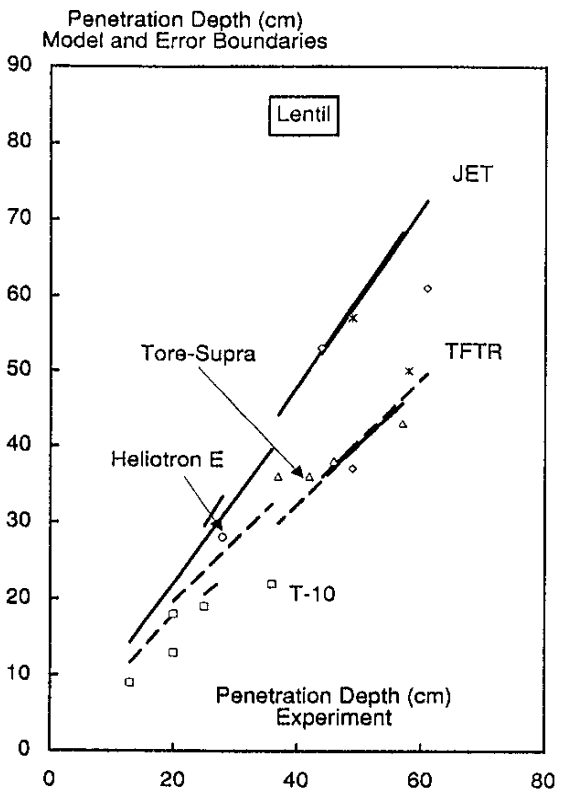

Fig.16 c

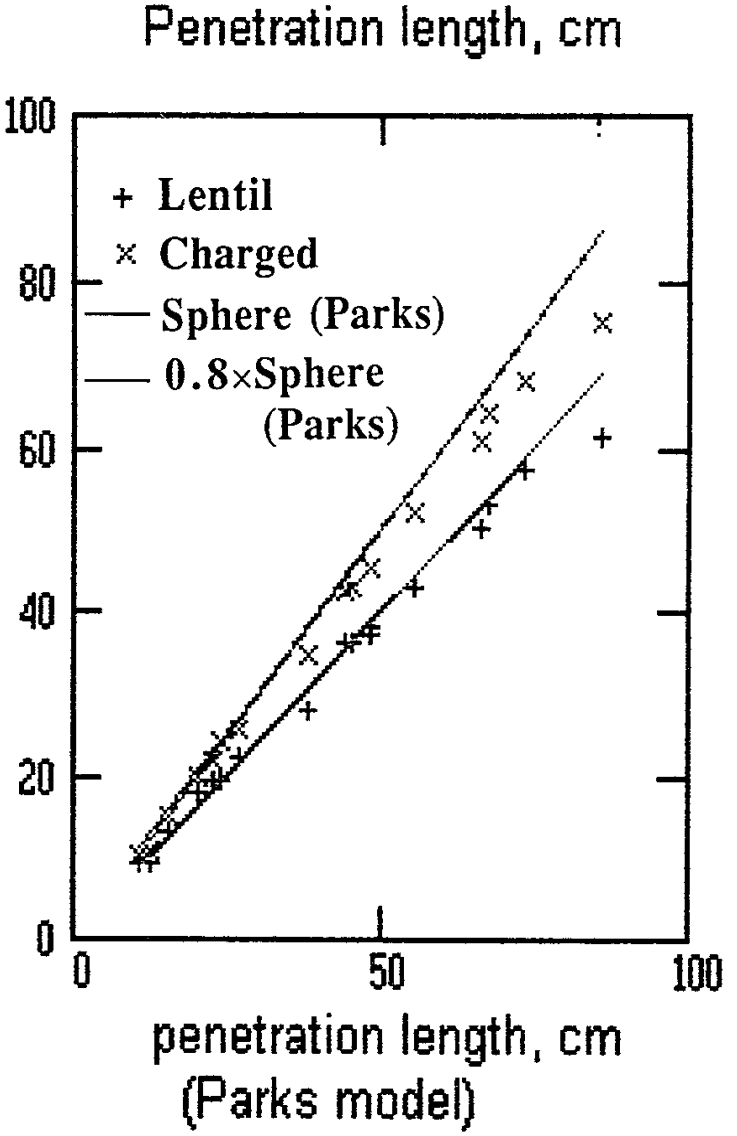
Penetration length, cm
100
80
60
40
20
0
+ Lentil
× Charged
Sphere (Parks)
0.8×Sphere (Parks)
0
50
100
penetration length, cm (Parks model)

Fig. 17

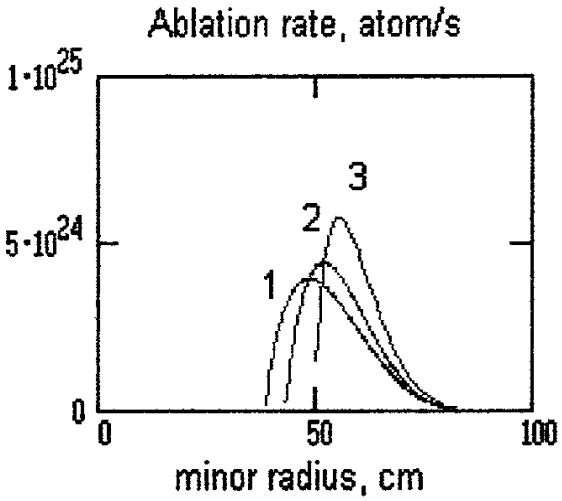
Ablation rate, atom/s
1·10^25
5·10^24
0
1
2
3
0
50
100
minor radius, cm

Fig.18

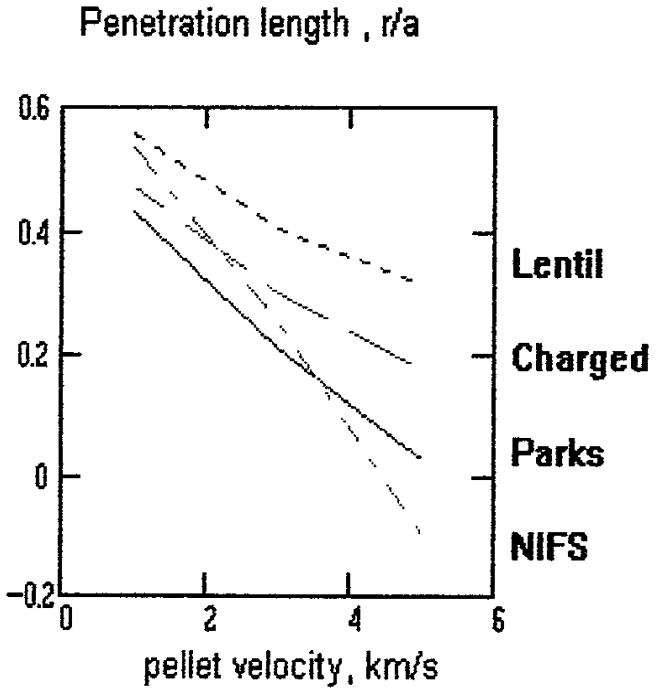
Penetration length , r/a
0.6
0.4
0.2
0
−0.2
0
2
4
6
pellet velocity, km/s
Lentil
Charged
Parks
NIFS

Fig.19

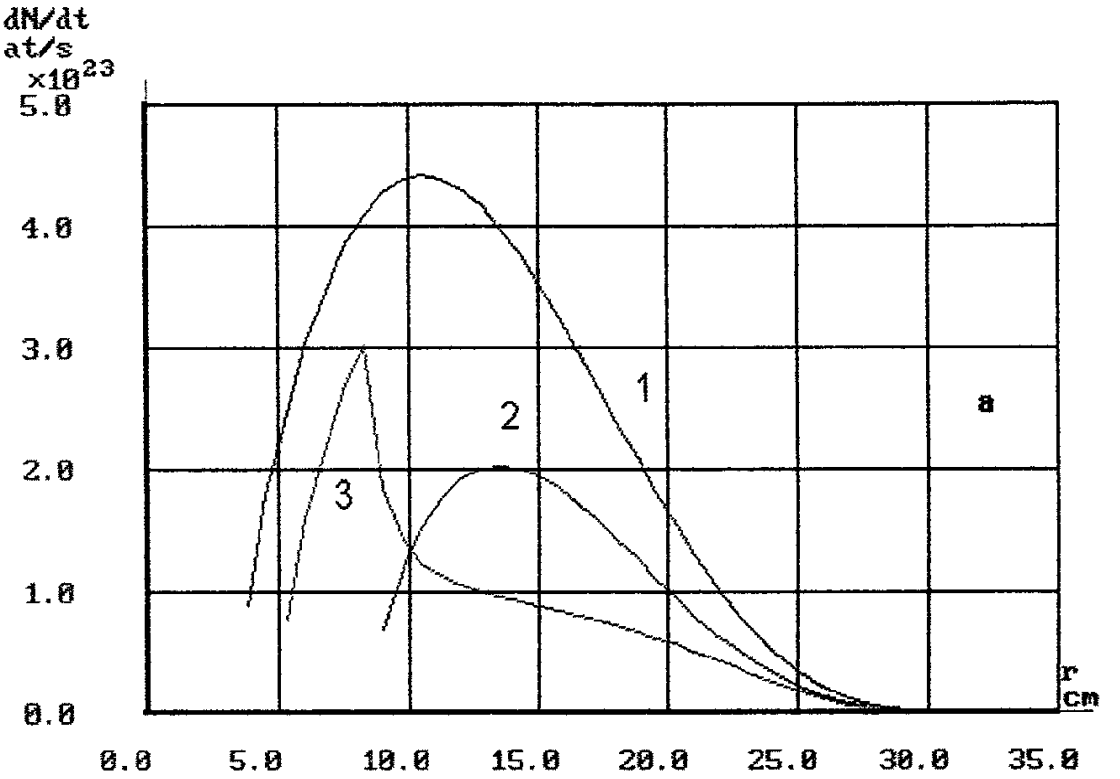

Fig. 20 a

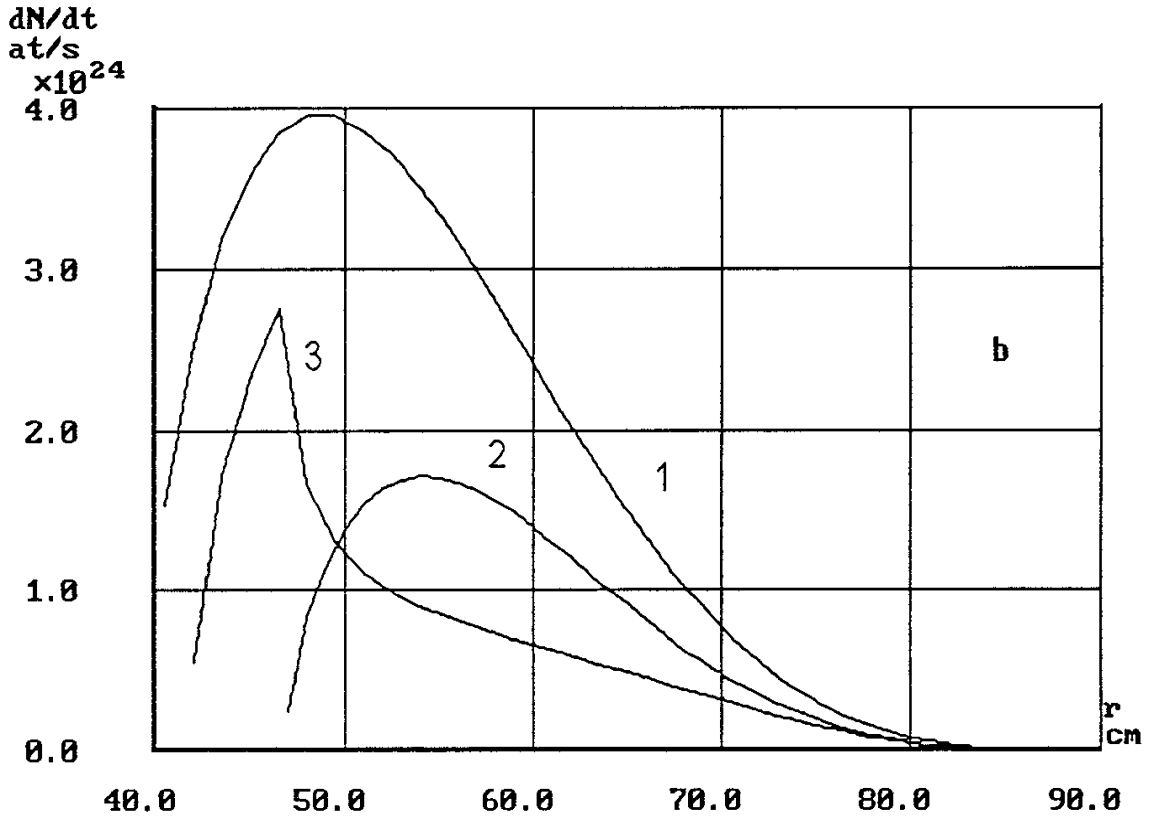

Fig. 20 b

Recent Issues of NIFS Series

NIFS-209 K. Masai, *Density Dependence of Line Intensities and Application to Plasma Diagnostics*; Feb. 1993

NIFS-210 K. Ohkubo, M. Hosokawa, S. Kubo, M. Sato, Y. Takita and T. Kuroda, *R&D of Transmission Lines for ECH System* ; Feb. 1993

NIFS-211 A. A. Shishkin, K. Y. Watanabe, K. Yamazaki, O. Motojima, D. L. Grekov, M. S. Smirnova and A. V. Zolotukhin, *Some Features of Particle Orbit Behavior in LHD Configurations*; Mar. 1993

NIFS-212 Y. Kondoh, Y. Hosaka and J.-L. Liang, *Demonstration for Novel Self-organization Theory by Three-Dimensional Magnetohydrodynamic Simulation*; Mar. 1993

NIFS-213 K. Itoh, H. Sanuki and S.-I. Itoh, *Thermal and Electric Oscillation Driven by Orbit Loss in Helical Systems*; Mar. 1993

NIFS-214 T. Yamagishi, *Effect of Continuous Eigenvalue Spectrum on Plasma Transport in Toroidal Systems*; Mar. 1993

NIFS-215 K. Ida, K. Itoh, S.-I.Itoh, Y. Miura, JFT-2M Group and A. Fukuyama, *Thickness of the Layer of Strong Radial Electric Field in JFT-2M H-mode Plasmas*; Apr. 1993

NIFS-216 M. Yagi, K. Itoh, S.-I. Itoh, A. Fukuyama and M. Azumi, *Analysis of Current Diffusive Ballooning Mode*; Apr. 1993

NIFS-217 J. Guasp, K. Yamazaki and O. Motojima, *Particle Orbit Analysis for LHD Helical Axis Configurations* ; Apr. 1993

NIFS-218 T. Yabe, T. Ito and M. Okazaki, *Holography Machine HORN-1 for Computer-aided Retrieve of Virtual Three-dimensional Image* ; Apr. 1993

NIFS-219 K. Itoh, S.-I. Itoh, A. Fukuyama, M. Yagi and M. Azumi, *Self-sustained Turbulence and L-Mode Confinement in Toroidal Plasmas* ; Apr. 1993

NIFS-220 T. Watari, R. Kumazawa, T. Mutoh, T. Seki, K. Nishimura and F. Shimpo, *Applications of Non-resonant RF Forces to Improvement of Tokamak Reactor Performances Part I: Application of Ponderomotive Force* ; May 1993

NIFS-221 S.-I. Itoh, K. Itoh, and A. Fukuyama, *ELMy-H mode as Limit Cycle and Transient Responses of H-modes in Tokamaks* ; May 1993

NIFS-222 H. Hojo, M. Inutake, M. Ichimura, R. Katsumata and T. Watanabe, *Interchange Stability Criteria for Anisotropic Central-Cell Plasmas in the Tandem Mirror GAMMA 10 ;* May 1993

NIFS-223 K. Itoh, S.-I. Itoh, M. Yagi, A. Fukuyama and M. Azumi, *Theory of Pseudo-Classical Confinement and Transmutation to L-Mode;* May 1993

NIFS-224 M. Tanaka, *HIDENEK: An Implicit Particle Simulation of Kinetic-MHD Phenomena in Three-Dimensional Plasmas;* May 1993

NIFS-225 H. Hojo and T. Hatori, *Bounce Resonance Heating and Transport in a Magnetic Mirror;* May 1993

NIFS-226 S.-I. Iton, K. Itoh, A. Fukuyama, M. Yagi, *Theory of Anomalous Transport in H-Mode Plasmas;* May 1993

NIFS-227 T. Yamagishi, *Anomalous Cross Field Flux in CHS ;* May 1993

NIFS-228 Y. Ohkouchi, S. Sasaki, S. Takamura, T. Kato, *Effective Emission and Ionization Rate Coefficients of Atomic Carbons in Plasmas;* June 1993

NIFS-229 K. Itoh, M. Yagi, A. Fukuyama, S.-I. Itoh and M. Azumi, *Comment on 'A Mean Field Ohm's Law for Collisionless Plasmas;* June 1993

NIFS-230 H. Idei, K. Ida, H. Sanuki, H. Yamada, H. Iguchi, S. Kubo, R. Akiyama, H. Arimoto, M. Fujiwara, M. Hosokawa, K. Matsuoka, S. Morita, K. Nishimura, K. Ohkubo, S. Okamura, S. Sakakibara, C. Takahashi, Y. Takita, K. Tsumori and I. Yamada, *Transition of Radial Electric Field by Electron Cyclotron Heating in Stellarator Plasmas;* June 1993

NIFS-231 H.J. Gardner and K. Ichiguchi, *Free-Boundary Equilibrium Studies for the Large Helical Device,* June 1993

NIFS-232 K. Itoh, S.-I. Itoh, A. Fukuyama, H. Sanuki and M. Yagi, *Confinement Improvement in H-Mode-Like Plasmas in Helical Systems,* June 1993

NIFS-233 R. Horiuchi and T. Sato, *Collisionless Driven Magnetic Reconnection,* June 1993

NIFS-234 K. Itoh, S.-I. Itoh, A. Fukuyama, M. Yagi and M. *Azumi, Prandtl Number of Toroidal Plasmas;* June 1993

NIFS-235 S. Kawata, S. Kato and S. Kiyokawa , *Screening Constants for Plasma;* June 1993

NIFS-236 A. Fujisawa and Y. Hamada, *Theoretical Study of Cylindrical Energy Analyzers for MeV Range Heavy Ion Beam Probes;* July 1993

NIFS-237 N. Ohyabu, A. Sagara, T. Ono, T. Kawamura and O. Motojima, *Carbon Sheet Pumping;* July 1993

NIFS-238 K. Watanabe, T. Sato and Y. Nakayama, *Q-profile Flattening due to Nonlinear Development of Resistive Kink Mode and Ensuing Fast Crash in Sawtooth Oscillations;* July 1993

NIFS-239 N. Ohyabu, T. Watanabe, Hantao Ji, H. Akao, T. Ono, T. Kawamura, K. Yamazaki, K. Akaishi, N. Inoue, A. Komori, Y. Kubota, N. Noda, A. Sagara, H. Suzuki, O. Motojima, M. Fujiwara, A. Iiyoshi, *LHD Helical Divertor;* July 1993

NIFS-240 Y. Miura, F. Okano, N. Suzuki, M. Mori, K. Hoshino, H. Maeda, T. Takizuka, JFT-2M Group, K. Itoh and S.-I. Itoh, *Ion Heat Pulse after Sawtooth Crash in the JFT-2M Tokamak;* Aug. 1993

NIFS-241 K. Ida, Y.Miura, T. Matsuda, K. Itoh and JFT-2M Group, *Observation of non Diffusive Term of Toroidal Momentum Transport in the JFT-2M Tokamak;* Aug. 1993

NIFS-242 O.J.W.F. Kardaun, S.-I. Itoh, K. Itoh and J.W.P.F. Kardaun, *Discriminant Analysis to Predict the Occurrence of ELMS in H-Mode Discharges;* Aug. 1993

NIFS-243 K. Itoh, S.-I. Itoh, A. Fukuyama, *Modelling of Transport Phenomena;* Sep. 1993

NIFS-244 J. Todoroki, *Averaged Resistive MHD Equations;* Sep. 1993

NIFS-245 M. Tanaka, *The Origin of Collisionless Dissipation in Magnetic Reconnection;* Sep. 1993

NIFS-246 M. Yagi, K. Itoh, S.-I. Itoh, A. Fukuyama and M. Azumi, *Current Diffusive Ballooning Mode in Seecond Stability Region of Tokamaks;* Sep. 1993

NIFS-247 T. Yamagishi, *Trapped Electron Instabilities due to Electron Temperature Gradient and Anomalous Transport;* Oct. 1993

NIFS-248 Y. Kondoh, *Attractors of Dissipative Structure in Three Disspative Fluids;* Oct. 1993

NIFS-249 S. Murakami, M. Okamoto, N. Nakajima, M. Ohnishi, H. Okada,
Monte Carlo Simulation Study of the ICRF Minority Heating in the Large Helical Device; Oct. 1993

NIFS-250 A. Iiyoshi, H. Momota, O. Motojima, M. Okamoto, S. Sudo, Y. Tomita, S. Yamaguchi, M. Ohnishi, M. Onozuka, C. Uenosono,
Innovative Energy Production in Fusion Reactors; Oct. 1993

NIFS-251 H. Momota, O. Motojima, M. Okamoto, S. Sudo, Y. Tomita, S. Yamaguchi, A. Iiyoshi, M. Onozuka, M. Ohnishi, C. Uenosono,
Characteristics of D-^{3}He Fueled FRC Reactor: ARTEMIS-L, Nov. 1993

NIFS-252 Y. Tomita, L.Y. Shu, H. Momota,
Direct Energy Conversion System for D-^{3}He Fusion, Nov. 1993

NIFS-253 S. Sudo, Y. Tomita, S. Yamaguchi, A. Iiyoshi, H. Momota, O. Motojima, M. Okamoto, M. Ohnishi, M. Onozuka, C. Uenosono,
Hydrogen Production in Fusion Reactors, Nov. 1993

NIFS-254 S. Yamaguchi, A. Iiyoshi, O. Motojima, M. Okamoto, S. Sudo, M. Ohnishi, M. Onozuka, C. Uenosono,
Direct Energy Conversion of Radiation Energy in Fusion Reactor, Nov. 1993

NIFS-255 S. Sudo, M. Kanno, H. Kaneko, S. Saka, T. Shirai, T. Baba,
Proposed High Speed Pellet Injection System "HIPEL" for Large Helical Device
Nov. 1993

NIFS-256 S. Yamada, H. Chikaraishi, S. Tanahashi, T. Mito, K. Takahata, N. Yanagi, M. Sakamoto, A. Nishimura, O. Motojima, J. Yamamoto, Y. Yonenaga, R. Watanabe,
Improvement of a High Current DC Power Supply System for Testing the Large Scaled Superconducting Cables and Magnets; Nov. 1993

NIFS-257 S. Sasaki, Y. Uesugi, S. Takamura, H. Sanuki, K. Kadota,
Temporal Behavior of the Electron Density Profile During Limiter Biasing in the HYBTOK-II Tokamak; Nov. 1993

NIFS-258 K. Yamazaki, H. Kaneko, S. Yamaguchi, K.Y. Watanabe, Y.Taniguchi, O.Motojima, LHD Group,
Design of Central Control System for Large Helical Device (LHD); Nov. 1993

NIFS-259 K. Yamazaki, H. Kaneko, S. Yamaguchi, K.Y. Watanabe, Y.Taniguchi, O.Motojima, LHD Group,
Design of Central Control System for Large Helical Device (LHD); Nov. 1993